

The Atmosphere of Mars Analyzed by Integral Inversion of the Mariner IV Occultation Data

by

Gunnar Fjeldbo and Von R. Eshleman

November 1967

Final Report

FACILITY FORM 602

N68-16732	(THRU)
(ACCESSION NUMBER)	
61	(CODE)
(PAGES)	
C1-92718	30
(NASA CR OR TMX OR AD NUMBER)	(CATEGORY)

Prepared under
NASA Grant NGR-05-020-065

RADIOSCIENCE LABORATORY
STANFORD ELECTRONICS LABORATORIES
STANFORD UNIVERSITY • STANFORD, CALIFORNIA



THE ATMOSPHERE OF MARS ANALYZED BY INTEGRAL INVERSION
OF THE MARINER IV OCCULTATION DATA

by

Gunnar Fjeldbo and Von R. Eshleman

November 1967

FINAL REPORT

Prepared under

NASA Grant NGR-05-020-065

RadioScience Laboratory
Stanford Electronics Laboratories
Stanford University Stanford, California

PRECEDING PAGE BLANK NOT FILMED.

CONTENTS

	<u>Page</u>
1. INTRODUCTION	2
2. THE MARINER-MARS REFRACTIVITY PROFILES	3
3. THE LOWER ATMOSPHERE OF MARS	19
4. THE UPPER ATMOSPHERE OF MARS	36
5. CONCLUSIONS	46
APPENDIX A	48
APPENDIX B	52
REFERENCES	56

ILLUSTRATIONS

<u>Figure</u>	<u>Page</u>
1. Occultation geometry	4
2. Amplitude versus time during immersion.. . . .	6
3. Amplitude versus time during emersion	7
4. Refractivity profiles obtained from inversion of immersion doppler residuals	15
5. Atmospheric refractivity profiles for immersion and emersion	18
6. Refractivity profile for the lower atmosphere probed during immersion	20
7. Refractivity and number density versus altitude in the lower atmosphere probed during immersion	21
8. Refractivity profile for the lower atmosphere probed during emersion	25
9. Refractivity and number density versus altitude in the lower atmosphere probed during emersion	26
10. Temperature profiles for the lower atmosphere probed during immersion	30
11. Temperature profiles for the lower atmosphere probed during emersion	32
12. Pressure profiles for immersion and emersion	34
13. Electron number density profile for the upper atmosphere probed during immersion	37
14. Plasma temperature profiles for the upper atmosphere probed during immersion	39
15. Number density versus altitude for three different atmos- pheric models	41
16. Temperature versus altitude for three different atmospheric models	42

ILLUSTRATIONS (cont.)

<u>Figure</u>	<u>Page</u>
17. Ray path geometry	49
18. Cross section of atmosphere consisting of K spherical layers	53

THE ATMOSPHERE OF MARS ANALYZED BY INTEGRAL INVERSION
OF THE MARINER IV OCCULTATION DATA

Gunnar Fjeldbo and Von R. Eshleman

Center for Radar Astronomy, Stanford University, Stanford, California

Abstract - The aim of this paper is to present results of a detailed analysis of the Mariner IV radio occultation data, using the data as directly as possible with a minimum number of assumptions and interpretations. Integral inversion of the basic measurements is used to obtain height profiles of refractivity over the immersion and emersion points on Mars. For the upper atmosphere this yields directly the ionospheric profile, from which a profile representing plasma temperature divided by mean molecular mass is derived assuming either diffusive or photoionization equilibrium conditions. Molecular number density, temperature, and pressure profiles for the lower atmosphere are derived for two constituent models assuming only mixed, non-polar molecules in hydrostatic equilibrium. It is believed that rather high precision has been obtained for conditions at the immersion point, but that the emersion results are less precise due to a change in the mode of operation of the radio system.

1. INTRODUCTION

The initial analyses of the Mariner IV occultation data were based primarily on model fitting; i.e., the parameters of an assumed model for the atmosphere refractivity profile were adjusted so as to minimize the differences between the computed and the measured radio phase changes [Kliore et al, 1965]. (The refractivity N of a medium is defined as $(n-1) 10^6$, where n is the refractive index.) The model fitting approach becomes impractical, however, if one wants to utilize the data to study the finer structure of the atmosphere. Under these circumstances, the fitting technique requires the use of so many variable parameters that it is easier to invert the integral equation relating the radio phase measurements to the atmospheric refractivity profile (Fjeldbo and Eshleman, 1965). The refractivity profile obtained from inversion can be considered the ideal model fit with standard deviation (or goodness) of fit equal to zero.

We have now completed a more detailed study of both the phase and amplitude data provided by Mariner IV, and have utilized integral inversion to calculate the atmospheric refractivity as a function of height at both occultation immersion and emersion. This work is summarized in Sec. 2. In Secs. 3 and 4, we use the measured refractivity profiles to derive molecular number density, temperature, and pressure profiles for the lower atmosphere, and electron number density and plasma temperature profiles for the upper atmosphere.

2. THE MARINER-MARS REFRACTIVITY PROFILES

Reception at the NASA Deep Space Network of the tracking and telemetry signal from the Mariner IV spacecraft provided the basic data. Before describing the analysis of the data, we shall briefly review the measurements. (A more complete description of the instrumentation has been given by G. S. Levy et al, 1966.)

The geometry of the experiment is illustrated in Fig. 1. During immersion, the radio receiver on the spacecraft was phase-locked to the 2.1 Gc/sec uplink signal transmitted from Station 11 at Goldstone, California. The received signal was coherently translated to approximately 2.3 Gc/sec and transmitted back to earth where it was received at Stations 11 and 12 at Goldstone, and at two stations in Australia. In order to provide precise doppler measurements at Station 11, the received "downlink" signal was compared with the same rubidium frequency source as was used in the transmission. Similar frequency standards were employed at the other receiving terminals.

A different experimental configuration prevailed at emersion. At this time, the spacecraft transmitter derived its signal from a local oscillator which is less stable than the frequency standards on the earth. An attempt was made to lock up the spacecraft transponder to the uplink signal so that two-way doppler could be obtained instantly upon emersion. However, after end of occultation of the downlink signal, approximately 7.5 seconds of time elapsed before the spacecraft transponder went into lock. This unfortunate delay

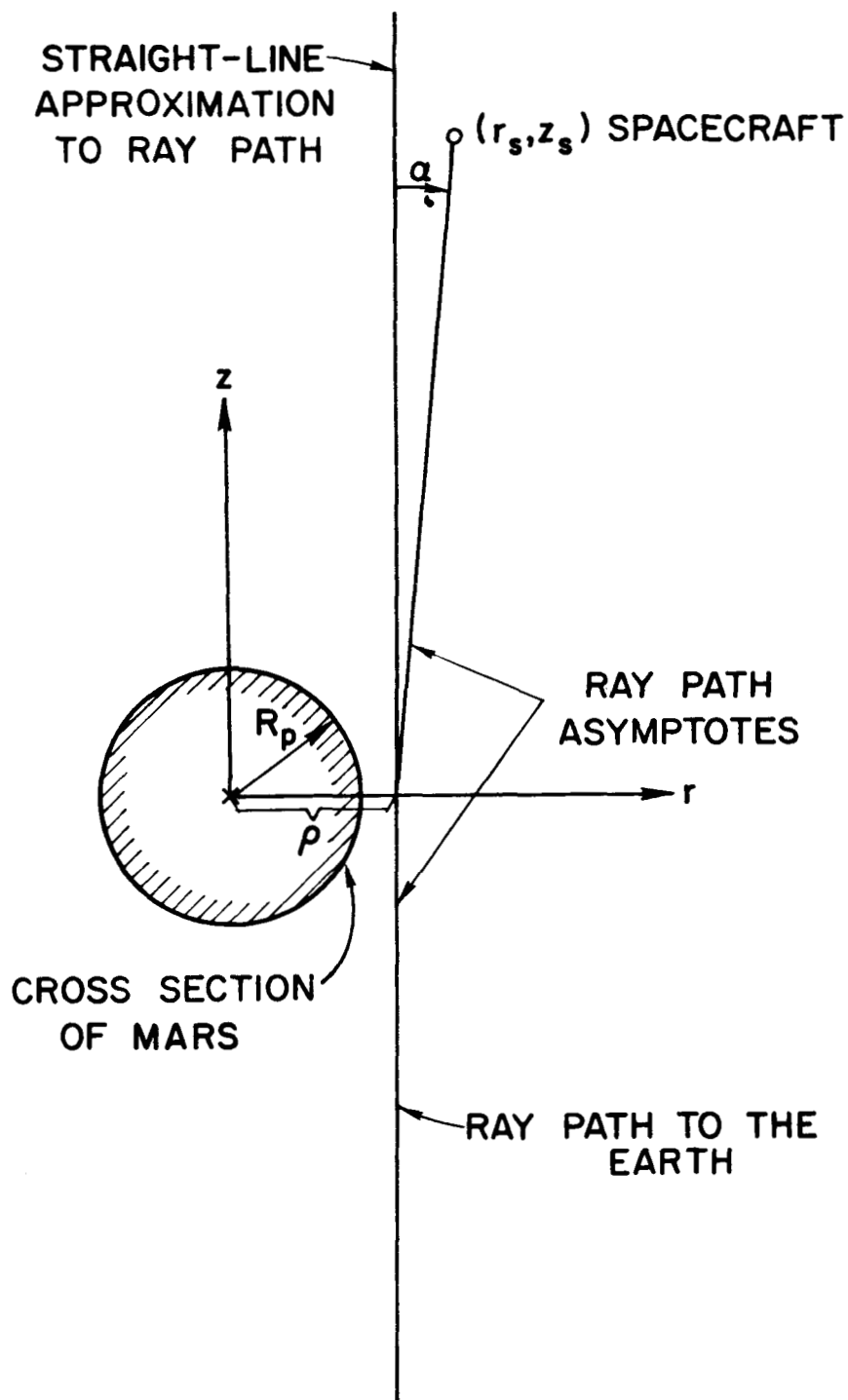


FIG. 1. OCCULTATION GEOMETRY. Immersion and emersion occurred 25,500 km and 39,200 km behind the Martian limb, respectively. The magnitude of the radial velocity (dr_s/dt) was about 2 km/sec during occultation.

leaves an ambiguity in the first 7.5 sec of the emersion doppler data because the frequency of the spacecraft's local oscillator is not known with precision.

All the tracking stations involved in the occultation experiment had phase-locked receivers which provided information on signal power and frequency in real time. In addition, the two Goldstone stations were equipped with open loop receivers for analog recording of the signal. Both types of receivers yielded valuable data during immersion. However, only open loop recordings were obtained during emersion, because none of the ground based phase-locked receivers locked on to the downlink signal in time to provide atmospheric data (Levy et al, 1966).

Figures 2 and 3 illustrate the analysis that has been conducted on the amplitude of the downlink signals. The amplitude and relative time scales of computed straight-edge Fresnel diffraction patterns were adjusted until a least-squares fit was obtained to the amplitude data. The best-fit diffraction pattern obtained in this manner has a reduced amplitude and is stretched out in time. The amplitude reduction is caused by defocussing (differential atmospheric refraction). The stretch of the Fresnel diffraction pattern is also related to the differential refraction (Fjeldbo and Eshleman, 1965).

The immersion data shown in Fig. 2 have been normalized with respect to the amplitude measured before the spacecraft was occulted by the Martian atmosphere. Thus, assuming that the system gain remained

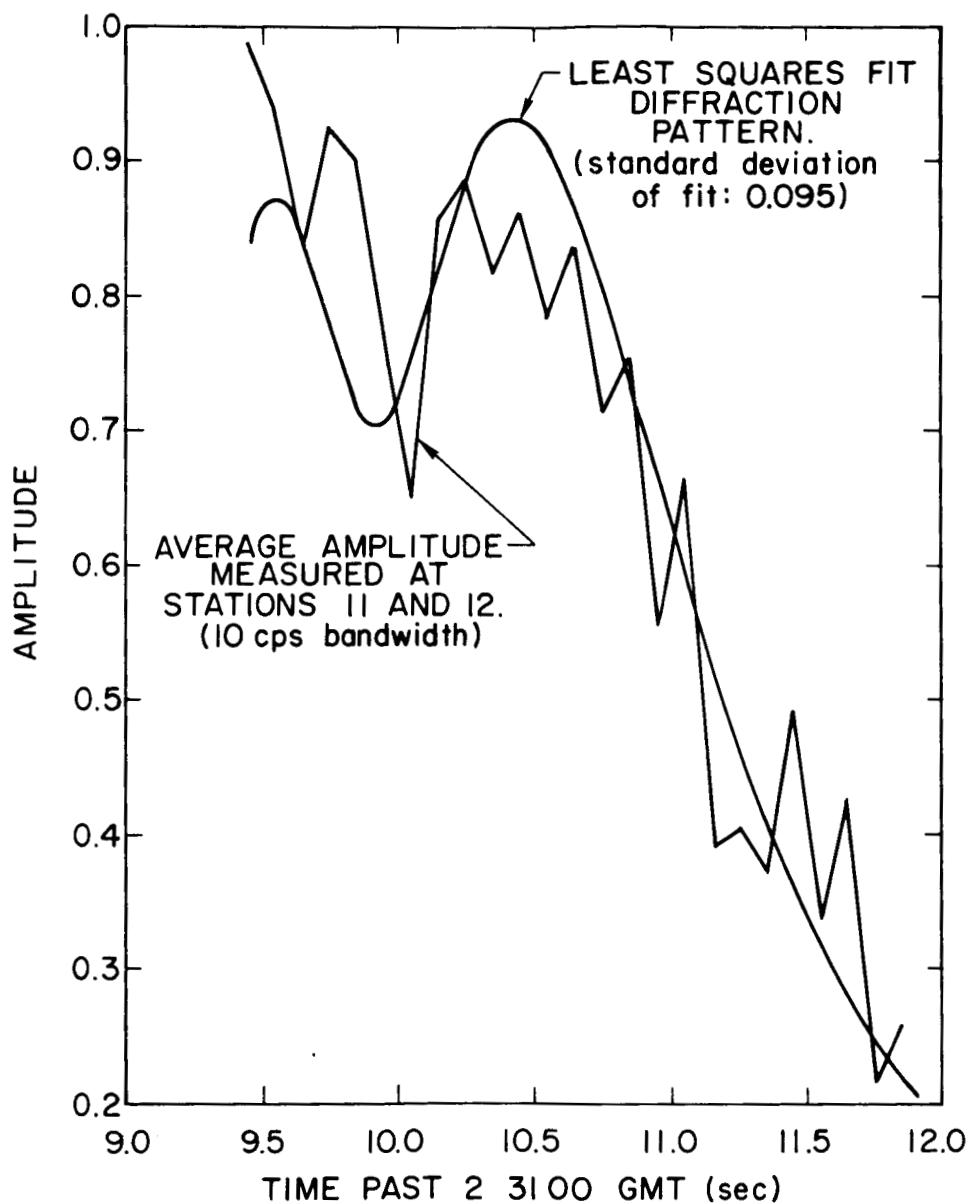


FIG. 2. AMPLITUDE VERSUS TIME DURING IMMERSION. The downlink grazed the Martian limb at $2^h 31^m 11.35^s \pm 0.15^s$ GMT; at this time the atmosphere had reduced the signal level by 2 db and produced a Fresnel stretch of 20%.

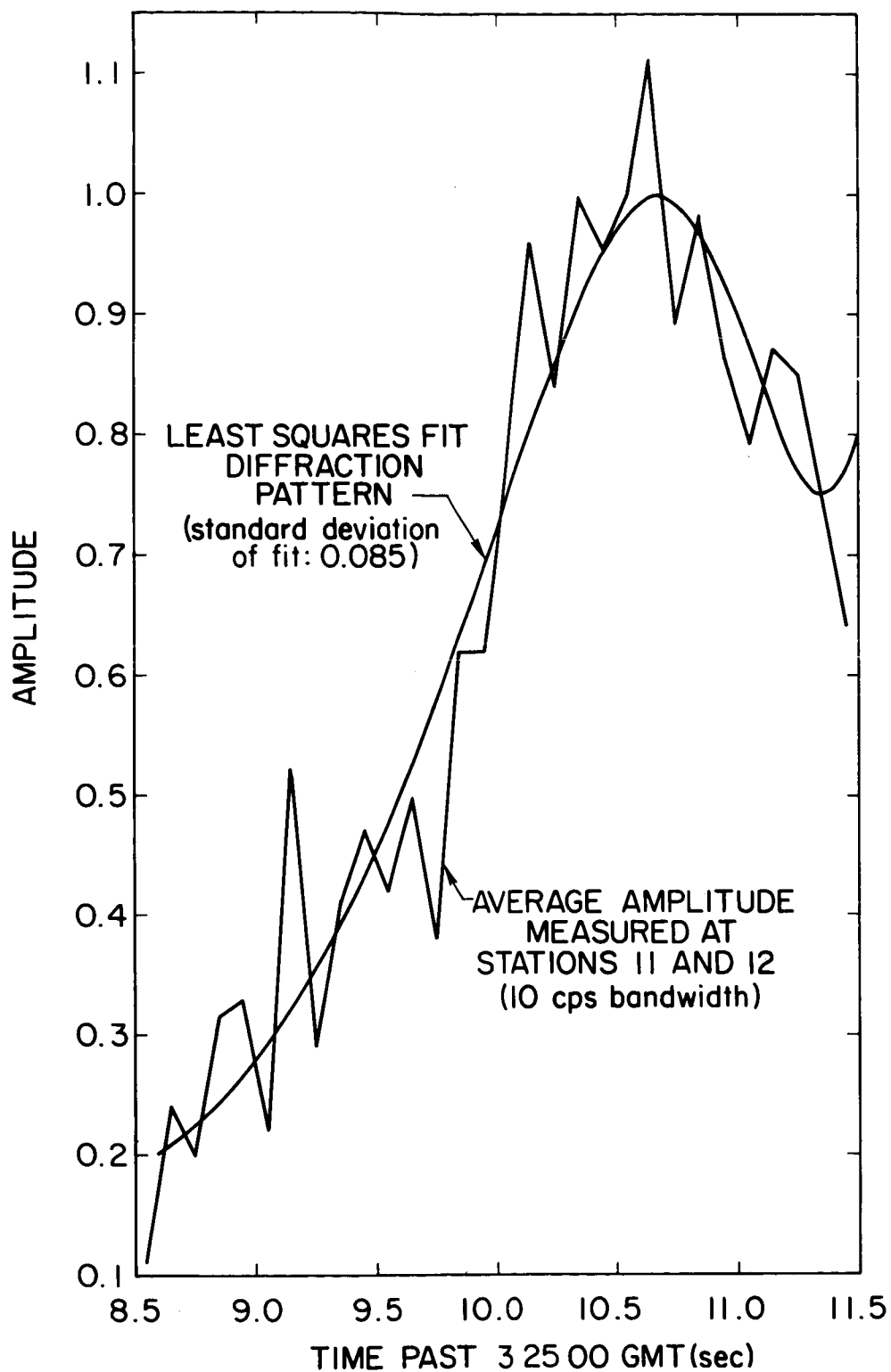


FIG. 3. AMPLITUDE VERSUS TIME DURING EMERSION. The downlink grazed the Martian limb at $3^h 25^m 9.45^s \pm 0.15^s$; at this time, the atmosphere had reduced the signal level by about 1.5 db and produced a Fresnel stretch of 30%.

unchanged during the measurements, the reduction in signal intensity (approximately 2 db) given by the least-squares fit curve in Fig. 2, is attributable to the Martian atmosphere. (For comparison, we computed the defocussing corresponding to the refractivity profile determined from the phase measurements and obtained a value of 2.1 db for grazing ray conditions. For the Fresnel stretch, the amplitude data gave 20%, while calculations based on the refractivity profile determined from the phase measurements gave 27%).

The amplitude data for emersion, shown in Fig. 3, have been normalized with respect to the signal amplitude measured after the spacecraft emerged from behind the Martian atmosphere. We have also attempted to account for a change in the system gain associated with the transition from one-way to two-way modes of operation. This complication makes the measurements of the atmospheric defocussing less precise for emersion than for immersion.

The signal-to-noise ratio was only about 10 db in a 10 cps bandwidth during the occultation measurements. However, within the experimental uncertainties, the results from atmospheric defocussing and Fresnel stretch are in agreement with the refractivity profiles deduced from the phase changes of the signal. Thus the amplitude data provide an important check and verification of the phase data, but are less precise for determining atmospheric parameters.

The most important role of the amplitude analysis, however, is to provide the precise times at which the downlink signal grazed the Martian limbs. These times are used to determine the surface levels in the analysis of the immersion and emersion phase data, and for deducing planetary radii. Using the data both for immersion and emersion together with the trajectory coordinates provided by the orbit determination group of the Jet Propulsion Laboratory, we find a mean radius of about 3381 km for the two occultation points. The radius at immersion appears to be about 5 km greater than that at emersion, but the uncertainty in the difference is comparable with this value.

Next, we will describe briefly how the refractivity profiles were computed from the frequency perturbations measured with the radio link. The total doppler shift is due both to changes in geometrical distance between tracking stations on earth and the spacecraft (range rate doppler), and to changes in the refractive index along the changing propagation paths. The trajectory of the spacecraft is computed from doppler frequency measurements taken throughout the flight, including the time near encounter but excluding the time when the signals were perturbed by the atmosphere of Mars. Subtracting computed range rate doppler from measured doppler frequencies during encounter leaves residuals which are primarily due to the Martian atmosphere (Kliore et al, 1965). Remaining corrections for oscillator drift, the imperfect trajectory, and for other changes of refractivity in the atmosphere of the earth and in the interplanetary medium, are approximated by subtracting the very small,

constant-frequency term needed to make the doppler residuals equal zero at times near encounter. A final, even smaller correction is made after the data are inverted, by setting the zero reference of refractivity above the ionospheric or atmospheric region being studied.

From the trajectory coordinates and the doppler residuals (Δf) , the angle of refraction (α) of the propagation path is computed as a function of r_s . For small bending, α is given by:

$$\alpha = -\Delta f \lambda \left(\frac{dr_s}{dt} \right)^{-1} \quad (1)$$

where λ is the free space wavelength and dr_s/dt is the radial velocity of the spacecraft. The geometrical quantities involved are illustrated in Fig. 1. The corresponding distance by which the propagation path missed the center of Mars (ρ) is given by

$$\rho = r_s - z_s \alpha - \frac{z_s r_s}{D} \quad (2)$$

where r_s and z_s are the spacecraft coordinates defined in Fig. 1, and D is the distance between the spacecraft and the earth. Both Eq. 1 and Eq. 2 are based on the assumption that the angle of refraction (α) is small. The maximum bending imposed on the radio link by the Martian atmosphere was about 0.2 milliradians.

The transit time for the signal traveling from the spacecraft to the earth was about 12 minutes during the occultation measurements. At any one time, the coordinate system shown in Fig. 1 was chosen so that the z-axis passed through the position which the earth-based receiver would occupy 12 minutes later. The origin of the coordinate system was chosen at the Martian center of mass.

Let ϕ denote the atmospheric perturbations of the phase path between Mariner and the earth. For immersion, $\phi(t)$ is given by

$$\phi(t) = - \int_{t_1}^t \Delta f \, dt \quad (\text{cycles}) \quad (3)$$

where t_1 denotes a time prior to Mariner's occultation by the Martian atmosphere. The minus sign implies that the doppler shift is negative when $\phi(t)$ is increasing with time. Similarly, we have for emersion:

$$\phi(t) = \int_t^{t_2} \Delta f \, dt \quad (\text{cycles}) \quad (4)$$

where t_2 denotes a time after the spacecraft to earth path cleared the atmosphere of Mars during emersion.

The phase changes ϕ can conveniently be considered a superposition of two effects; namely the change (ϕ_1) introduced because the refractivity differs from zero along that portion of the radio link

which is passing through the atmosphere, plus the phase path increase $(\alpha^2 z_s^2 / 2\lambda)$ associated with the bending of the propagation path. Thus, we have

$$\phi_1 = \phi - \frac{\alpha^2 z_s^2}{2\lambda} \quad (5)$$

Equations 1 through 5 may be utilized to calculate ϕ_1 as a function of ρ . The function $\phi_1(\rho)$ is again related to the refractivity $N(r)$ by

$$\phi_1(\rho) = \frac{10^{-6}}{\lambda} \int_{-\infty}^{+\infty} N(r) \, dz \quad (6)$$

where

$$r = \sqrt{\rho^2 + z^2}.$$

Equations (5) and (6) are based on the assumption that the refractive bending is small and the propagation path has been approximated with a straight line in the region where $N(r)$ differs from zero. For a more detailed description of the approximations utilized here, the reader is referred to Appendix A.

There are several techniques that may be utilized to compute $N(r)$ from $\phi_1(\rho)$ (Fjeldbo, 1964). The method to be outlined here was chosen

because it does not require any pre-inversion filtering of the raw doppler residual data. This approach may offer three advantages:

(1) the refractivity profiles are available in a form where the altitude resolution is unaffected by any particular filter characteristics (other than the 12 cps phase-locked-loop bandwidth); (2) post-inversion filtering may require less computer time since it is unnecessary to repeat the inversion computations if one wants to change the filter; (3) the physical properties of the atmosphere are related more simply to the parameters of a matched filter applied to $N(h)$ than to the doppler data.

Let K denote the number of data points describing $\phi_1(\rho)$. In brief, Eq. 6 may be inverted by dividing the atmosphere into K spherical layers each having constant refractivity. Starting with $\phi_1(\rho)$ for the ray that is passing tangentially through the top layer, one computes the refractivity of this layer by simply dividing $\lambda 10^6 \phi_1(\rho)$ by the corresponding path length. The second ray from the top is passing through two atmospheric layers. The effect the top layer has on $\phi_1(\rho)$ for this second ray can readily be subtracted. The remaining phase residual is divided by the length of that portion of the ray which is enclosed in the second layer. This calculation gives the refractivity of the second layer. Repeating these calculations for the remaining rays yields the entire refractivity profile. A more detailed description of this procedure is given in Appendix B.

Figure 4 shows some examples of the refractivity profiles that were computed from the doppler residuals provided by Mariner IV. The first five profiles were calculated from residuals obtained prior to occultation. These curves were included to illustrate the noise and bias levels; thus their altitude scales are only relative.

The last profile in Fig. 4 shows the Martian atmosphere probed during entry into occultation. The upper portion of this profile represents the ionosphere where the refractivity is negative and proportional to the electron number density. In the lower atmosphere, the refractivity is positive and linearly related to the number density of each constituent. It is expected that the negative ionospheric refractivity is inversely proportional in magnitude to the square of the radio frequency, while the positive atmospheric refractivity is essentially independent of the frequency.

All the profiles in Fig. 4 were obtained with the same data-processing techniques. In each case, the zero-reference level for the refractivity was set by subtracting any doppler bias that might remain after the gross effects of the trajectory are removed. This doppler bias was determined by taking the mean of the doppler residuals obtained in a one minute period just prior to the start of the profile. Thus all constant doppler bias that may have been produced by the radio system, the earth's atmosphere, the interplanetary medium, or by errors in the trajectory, has been removed.

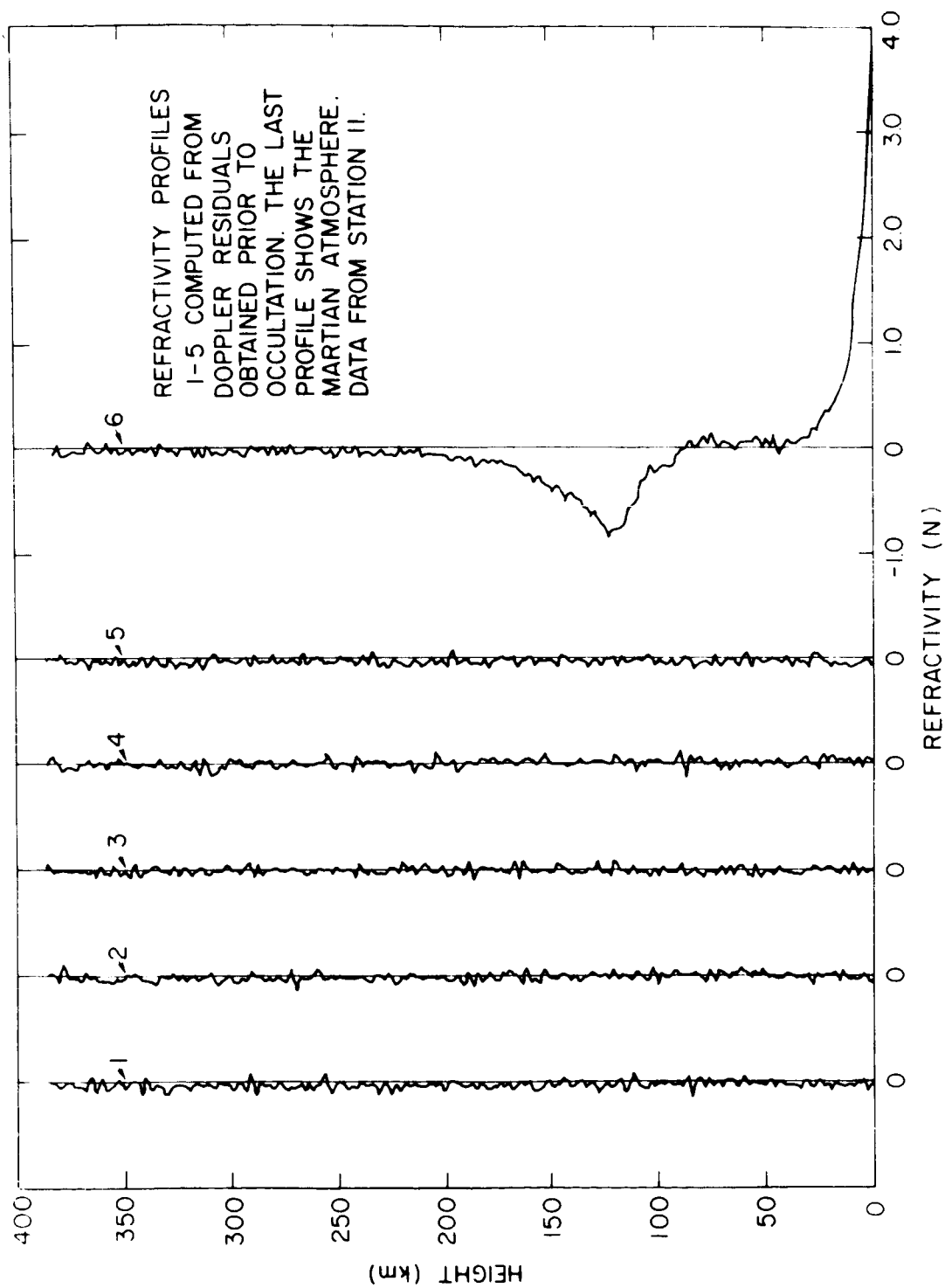


FIG. 4. REFRACTIVITY PROFILES OBTAINED FROM INVERSION OF IMMERSION DOPPLER RESIDUALS.

In the analysis of the two-way doppler, it was necessary to take into account that the uplink and the downlink did not follow precisely the same path through the Martian atmosphere. This effect was caused by changes in the direction to the earth as observed in an areocentric coordinate system fixed with respect to the stars. During the 24 minutes round-trip propagation time, the earth moved on the order of 0.1 milliradians causing the downlink to lag the uplink in sweeping through the Martian atmosphere. The altitude difference between the two propagation paths was on the order of two kilometers at Mars.

The complication introduced by having two different paths was handled by dividing the two-way doppler residuals by two and considering the propagation as one-way along a mean path located between the uplink and downlink. This approach is applicable in the atmospheric regions where the refractivity scale height is large compared to the altitude separation of the two radio links.

The residuals employed in calculating the profiles in Fig. 4 were obtained from the doppler measurements made with the phase-locked receiver system at Station 11. In this system, the phase of the radio signal was determined by cumulatively counting positive-going zero crossings. Once every second, the change in the zero crossing count was recorded to provide a measure of doppler frequency. The quantization errors were reduced by multiplying the doppler frequency by a factor of 8 prior to the counting (Levy et al, 1966).

Most of the noise on the refractivity profiles of Fig. 4 is due to the doppler quantization errors. The period or height interval of this refractivity noise is determined by the speed with which the radio link swept through the atmosphere, and is about 4 km in the upper atmosphere and about 3 km near the surface.

Figure 5 shows the immersion and emersion profiles obtained by inverting the doppler data from Station 12. The immersion measurements were made in the southern part of Electris near 50°S , 177°E , at about 1300 hours local time in late winter. The azimuth angle of the propagation path was about 115° measured from north towards east. Emersion occurred in the vicinity of the northern edge of Mare Acidalium near 60°N , 36°W , at about 2340 hours local time in late summer. The azimuth angle of the grazing radio link was 65° . The most apparent difference between the two profiles is that there was no detectable ionosphere on the night side of the planet.

The atmospheric refractivity is the basic quantity measured with the radio occultation experiment. In order to interpret these measurements in terms of number density, temperature and pressure profiles, it is necessary to know the constituents. This problem is discussed in the next sections.

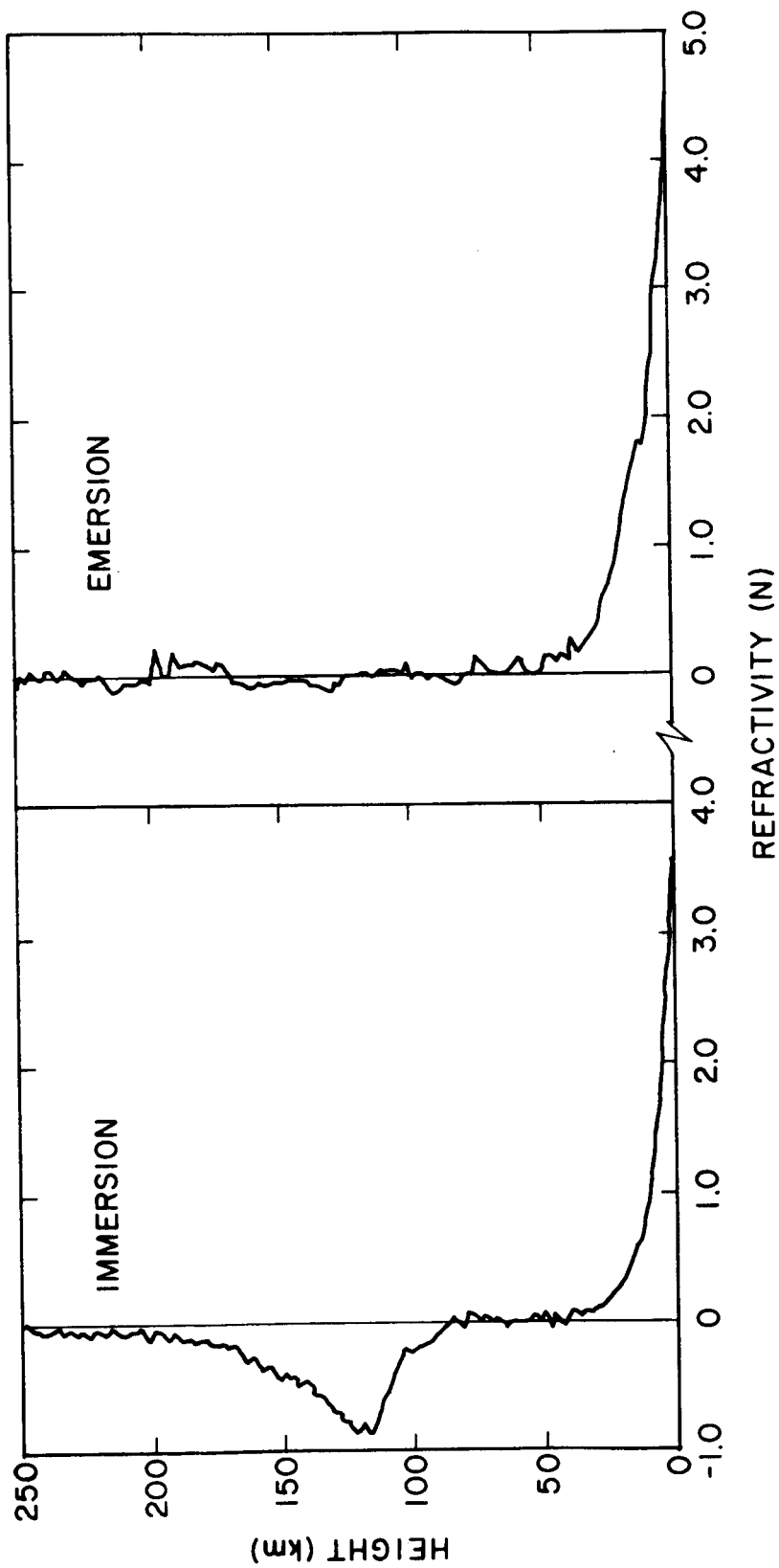


FIG. 5. ATMOSPHERIC REFRACTIVITY PROFILES FOR IMMERSION (near 50° S, 177° E, 1300 hours local time, late winter) AND EMERSION (near 60° N, 36° W, 2340 hours local time, late summer). The immersion and emersion measurements were made with closed and open loop receivers, respectively.

3. THE LOWER ATMOSPHERE OF MARS

Occultation measurements at a single radio frequency can not in general discriminate between free electrons and neutral constituents (Fjeldbo et al, 1965; Harrington et al, 1967). There are two ways in which the effects of ionized and neutral constituents might interfere. Electrons in the lower atmosphere would contribute directly to the refractivity profile for this region, and an ionosphere at greater height could affect the derived profile for the lower atmosphere if the ionosphere departs sensibly from spherical symmetry in the region probed by the radio waves. However, the shapes of the profiles in Figures 4 and 5 have led us to believe that free electrons contribute negligibly to the refractivity measured in the lower atmosphere. For example, the dayside profile does not show any region with negative refractivity below 80-km altitude, and no ionosphere was detected on the nightside of the planet. In addition, the possible effect of the lack of spherical symmetry in the ionosphere appears small since the profiles show near-zero refractivity in the 50-80 km height region between the positive and negative refractivity regions.

The conclusion regarding the probable absence of plasma effects in the lower atmosphere is strengthened by a comparison with the conditions prevailing in our own atmosphere. Assuming that the free electron number densities in the lower atmosphere of Mars are comparable with those measured at the same neutral density levels in the terrestrial atmosphere, one can show that the refractivity

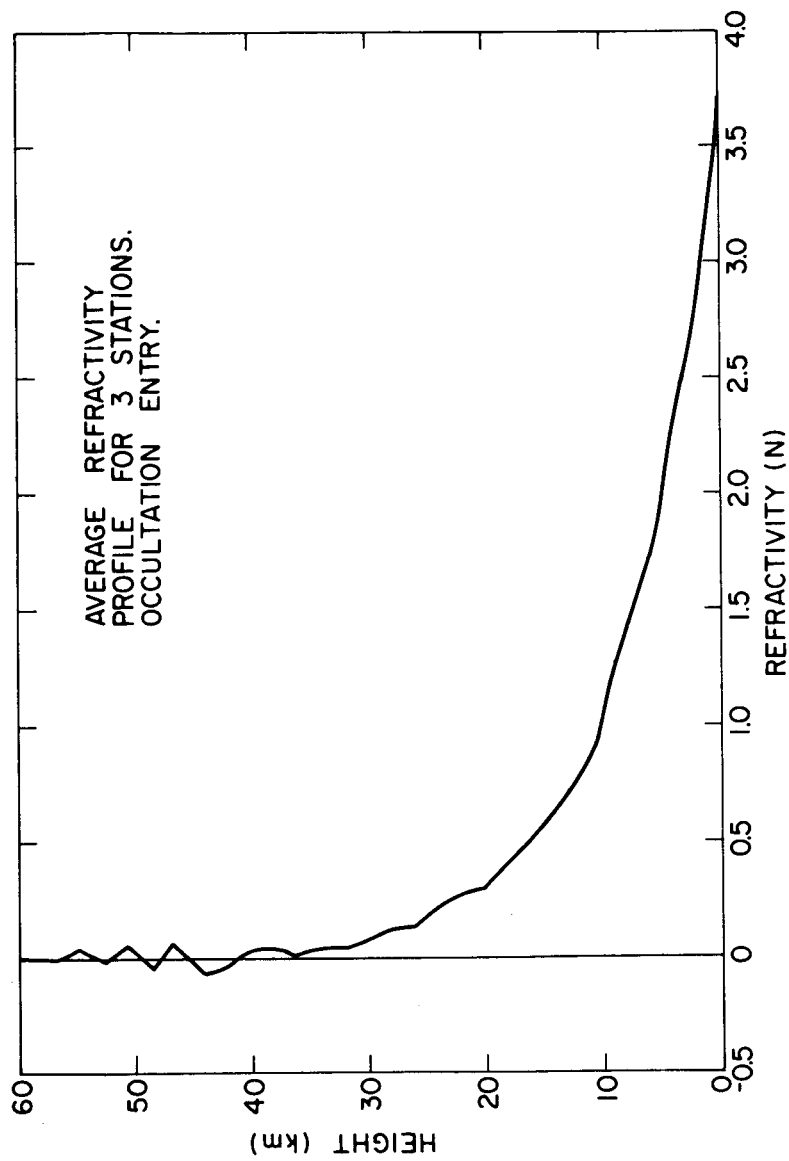


FIG. 6. REFRACTIVITY PROFILE FOR THE LOWER ATMOSPHERE PROBED DURING IMMERSION.

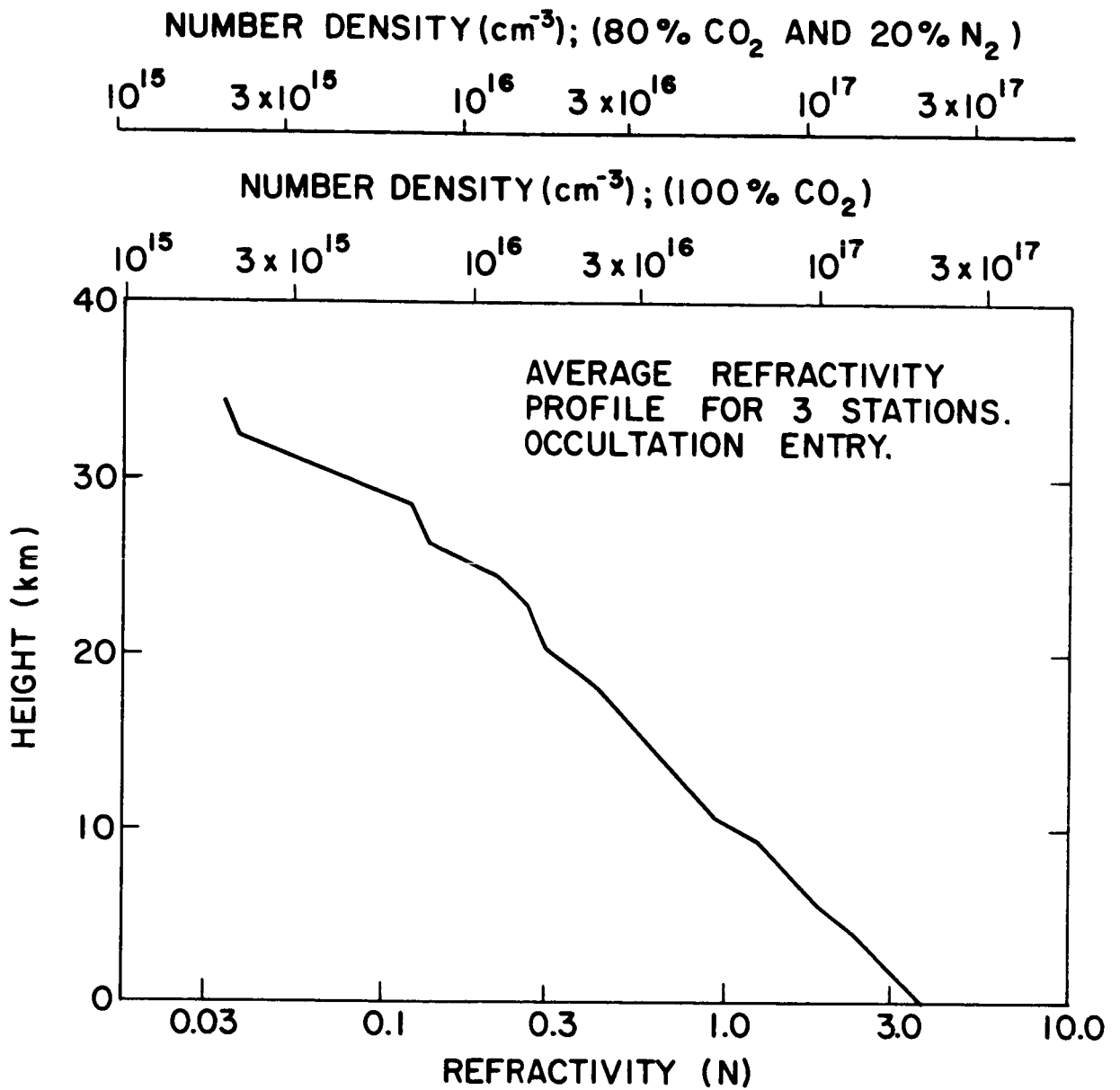


FIG. 7. REFRACTIVITY AND NUMBER DENSITY VERSUS ALTITUDE IN THE LOWER ATMOSPHERE PROBED DURING IMMERSION.

of the electrons is much smaller than that of the neutral gas. Thus, based on the evidence at hand, it seems plausible that free electrons have a negligible effect on the refractivity in the lower atmosphere of Mars.

Figures 6 and 7 show the refractivity measured in the lower atmosphere probed during immersion into occultation. The profile was obtained by averaging the refractivity measured at stations 11, 12, and 42. A slight positive refractivity bias in the 50 to 80-km height range (See Fig. 4) probably due either to random drifts of the frequency standards or to a very slight departure from spherical symmetry in the ionosphere, was subtracted in order to improve the zero reference.

A statistical analysis was made of the effect that changes in the refractivity bias may have had on the refractivity measurements in the lower atmosphere. In this analysis, we utilized refractivity profiles determined from doppler residuals obtained prior to occultation. (Cfr. Figure 4). These profiles were divided into layers of 40-km thickness (approximately the thickness of the detectable part of the lower atmosphere) and the refractivity bias was computed within each layer. The bias changed in a random manner from one layer to the next. However, the standard deviation in this change in the bias was only on the order of 0.01 refractivity units, which is about a third of one percent of the refractivity measured near the surface.

The last immersion doppler residual free of diffraction effects was measured when the mean radio path was approximately one km above the surface. Exponential extrapolation of the refractivity measurements down to the occultation point yields a surface refractivity of 3.7. The scale height of the refractivity profile measured during immersion is remarkably constant. A least-squares fit of the profile in Fig. 7 to an exponential function gives a scale height of 8 km. The standard deviation of the fit is 0.04 refractivity units which may be considered the formal error in the refractivity.

It is necessary to know the composition of the atmosphere before one can utilize the refractivity to determine the number density with precision. Fortunately, it appears that constituents are sufficiently well known to derive pressure, temperature, and density profiles with remarkably good precision. Ground-based infrared spectroscopic studies show that CO_2 may be the major constituent on Mars. They give a partial carbon dioxide pressure of 5 ± 2 mb (Belton and Hunten, 1966, Spinrad, et al 1966). The spectroscopic studies also yield the abundance of water vapor and upper limits for the abundance of O_2 , O_3 , CO , CH_4 , NH_3 , N_2O , NO_2 and a number of other gases (Rea, 1965) showing that none of these can contribute in a measurable way to the refractivity of the lower atmosphere of Mars. The most likely remaining candidates appear to be N_2 and A . Spectroscopic detection of these gases must be made in the ultraviolet and thus from outside the terrestrial atmosphere.

As an example of how to compute the number density from the

measured refractivity, let us assume that CO_2 , N_2 , and A are the only constituents in the lower atmosphere of Mars. The refractivity (N) of a mixture of these non-polar molecules is given by:

$$N = \left[1.84 \times 10^{-17} \frac{n_{\text{CO}_2}}{n_t} + 1.10 \times 10^{-17} \frac{n_{\text{N}_2}}{n_t} + 1.03 \times 10^{-17} \frac{n_A}{n_t} \right] n_t \quad (7)$$

where n_{CO_2} , n_{N_2} , and n_A denote the number density of CO_2 , N_2 , and A, respectively. The total number density of the gas is denoted n_t . The numerical coefficients in Eq. (7) have been determined from experimental data published by Essen and Froome (1951).

When the relative abundance of CO_2 , N_2 , and A are specified, one can utilize Eq. (7) to determine the total atmospheric number density (n_t). Two examples are shown in Fig. 7 where the two scales on the top of the graph give the number density for the case of 100% CO_2 and for the case of 80% CO_2 and 20% N_2 . The refractivity of N_2 and A are roughly the same; thus, it does not make much difference on the total number density whether the atmosphere contains 20% N_2 or a mixture of N_2 and A comprising 20% of the atmosphere.

Figures 8 and 9 show the corresponding refractivity and number density profile observed during emersion. This profile is ambiguous because one does not know exactly at what frequency the spacecraft was transmitting during the first 7.5 seconds of one-way measurements. Profile I was obtained by inverting the atmospheric doppler residual

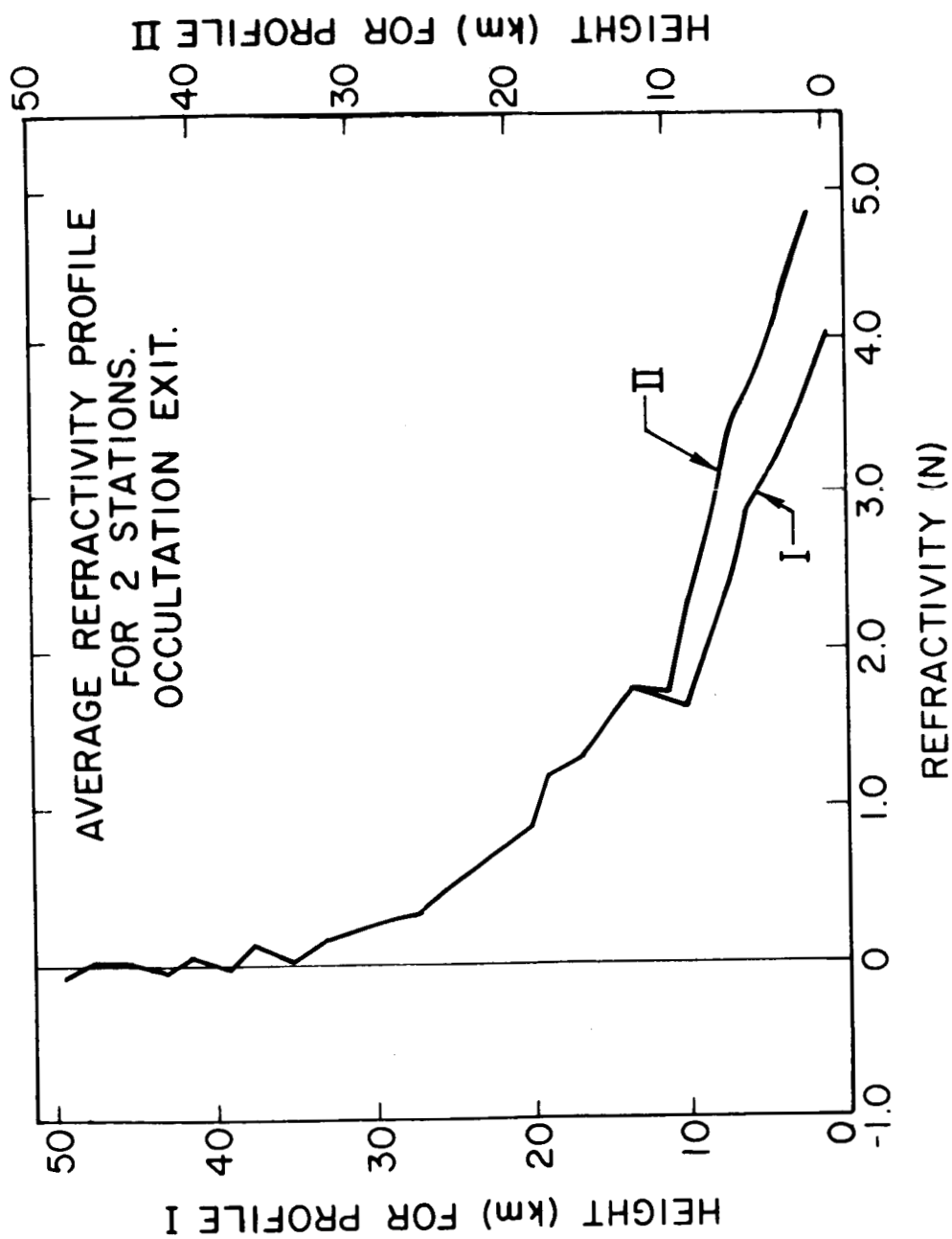


FIG. 8. REFRACTIVITY PROFILE FOR THE LOWER ATMOSPHERE PROBED DURING EMERSION.
Profile I and II were obtained by assuming different values for the space-
craft's local oscillator frequency.

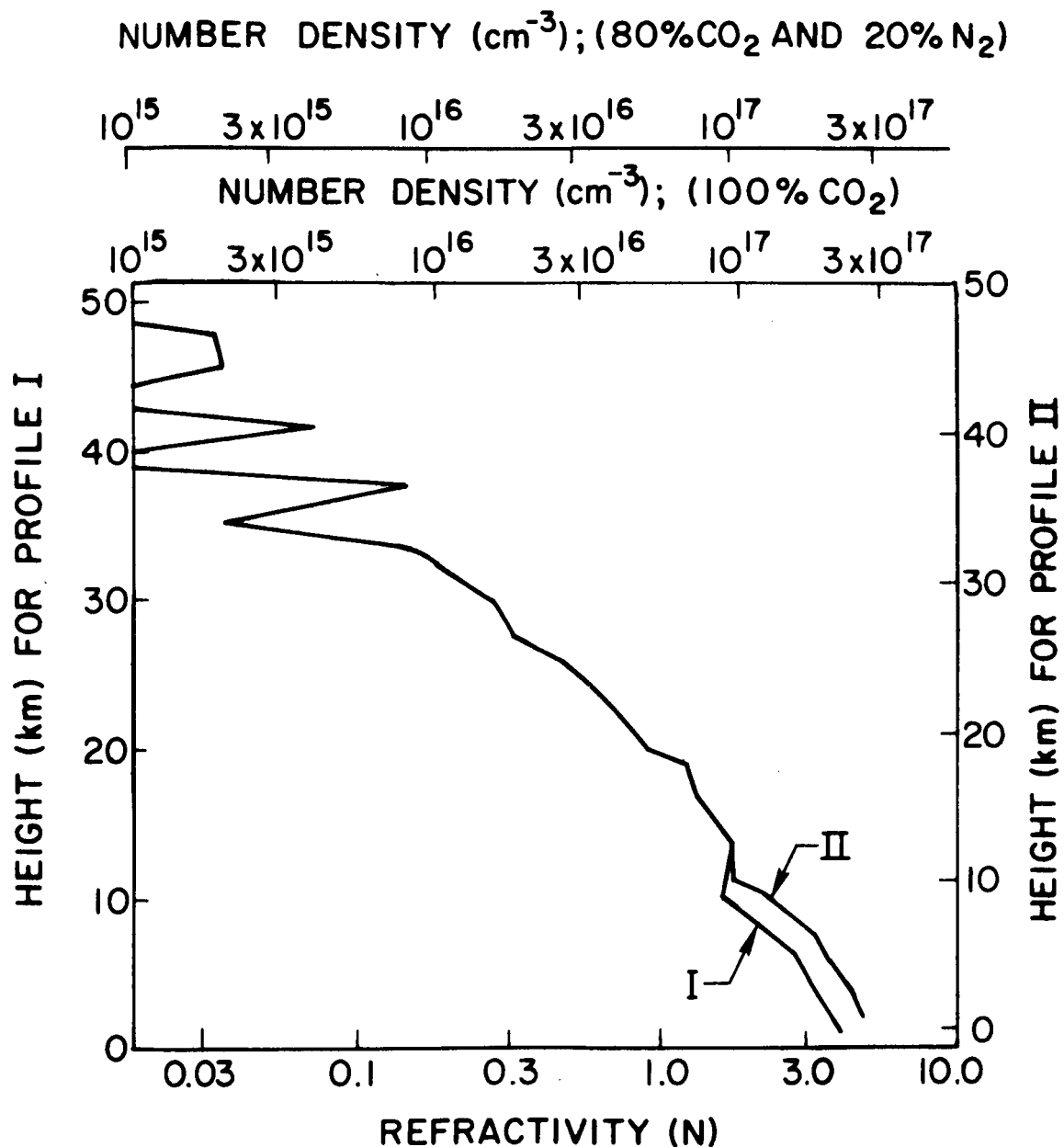


FIG. 9. REFRACTIVITY AND NUMBER DENSITY VERSUS ALTITUDE IN THE LOWER ATMOSPHERE PROBED DURING EMERSION.

data in the form published previously. (Levy et al, 1966, Fig. 28). Profile II was determined by inverting the same data but increasing the one way atmospheric doppler by 0.5 cps relative to the two way doppler. In other words, Profile II assumes that the frequency transmitted from the spacecraft during the first 7.5 seconds of emersion measurements was 0.5 cps lower than for Profile I. No unique solution exists below 10 km altitude and the two profiles shown in Fig. 8 and 9 result from an attempt to match doppler residuals across the discontinuity (Profile I) and to match refractivity across the discontinuity (Profile II).

The two profiles shown in Fig. 8 and 9 have a dip in the refractivity near 10 km altitude where the radio transponder changed from one-way to two-way mode of operation. A digital spectrum analysis of the downlink signal shows that the radio spectrum was somewhat broadened just prior to the change to two-way measurements. We believe this frequency broadening and the associated dip in the refractivity profile was produced by changes in the radio transponder system rather than by the the Martian atmosphere.

The refractivity measurements can also be utilized to study the thermal structure of the atmosphere. For an atmosphere in hydrostatic equilibrium, one can show that:

$$dp + n_t(h)\bar{m}(h)g(h) dh = 0 \quad (8)$$

where

$p(h)$ = pressure at altitude h

$dp = p(h + dh) - p(h)$

$n_t(h)$ = total number density

$\bar{m}(h)$ = mean molecular mass

$g(h)$ = acceleration of gravity ($g(0) \approx 3.75 \text{ m/sec}^2$)

dh = differential change in altitude.

The pressure in an ideal gas is given by

$$p(h) = k n_t(h) T(h) \quad (9)$$

where

k = Boltzmann's constant

$T(h)$ = temperature.

Eliminating $p(h)$ from Eqs. (8) and (9), and solving for

$T(h)$ yields

$$T(h) = T(h_o) \frac{n_t(h_o)}{n_t(h)} + \frac{1}{k n_t(h)} \int_h^{h_o} g(h) \bar{m}(h) n_t(h) dh \quad (10)$$

where h_o is the altitude at which the boundary value $T(h_o)$ is chosen.

In a well-mixed atmosphere, $n_t(h)$ is proportional to $N(h)$ and $\bar{m}(h)$ is independent of altitude. This simplification yields:

$$T(h) = T(h_o) \frac{N(h_o)}{N(h)} + \frac{\bar{m}}{kN(h)} \int_h^{h_o} g(h) N(h) dh \quad (11)$$

Figure 10 shows the results of employing this formula to compute temperature profiles for the atmospheric region probed during immersion. The calculations were performed by choosing five different boundary values at 30 km altitude and integrating downward towards the surface.

The value of the first term on the right-hand side of Eq. (11) depends upon the choice of boundary temperature $T(h_o)$, and is also affected by refractivity noise. Fortunately, however, the effect of this first term decreases rapidly with decreasing altitude since it is inversely proportional to $N(h)$. Thus, the uncertainty in the product $T(h_o) N(h_o)$ does not have a large effect on $T(h)$ at altitudes well below the boundary level (see Fig. 10).

Uncertainties in the refractivity bias also affect the temperature profiles. Changing the entire refractivity profile in the lower atmosphere by an amount equal to the standard deviation in the bias (± 0.01 refractivity units) yields a $\pm 2^\circ\text{K}$ change in the temperature near the surface (assuming 100% CO_2). The corresponding change in the surface pressure is approximately $\pm 2\%$.

The upper and lower temperature scales in Fig. 10 are for a mean molecular mass of 40.8 and 44.0, respectively. Assuming that CO_2 and N_2 are the only constituents, the two scales correspond to a pure CO_2 atmosphere and to a mixture of 80% CO_2 and 20% N_2 .

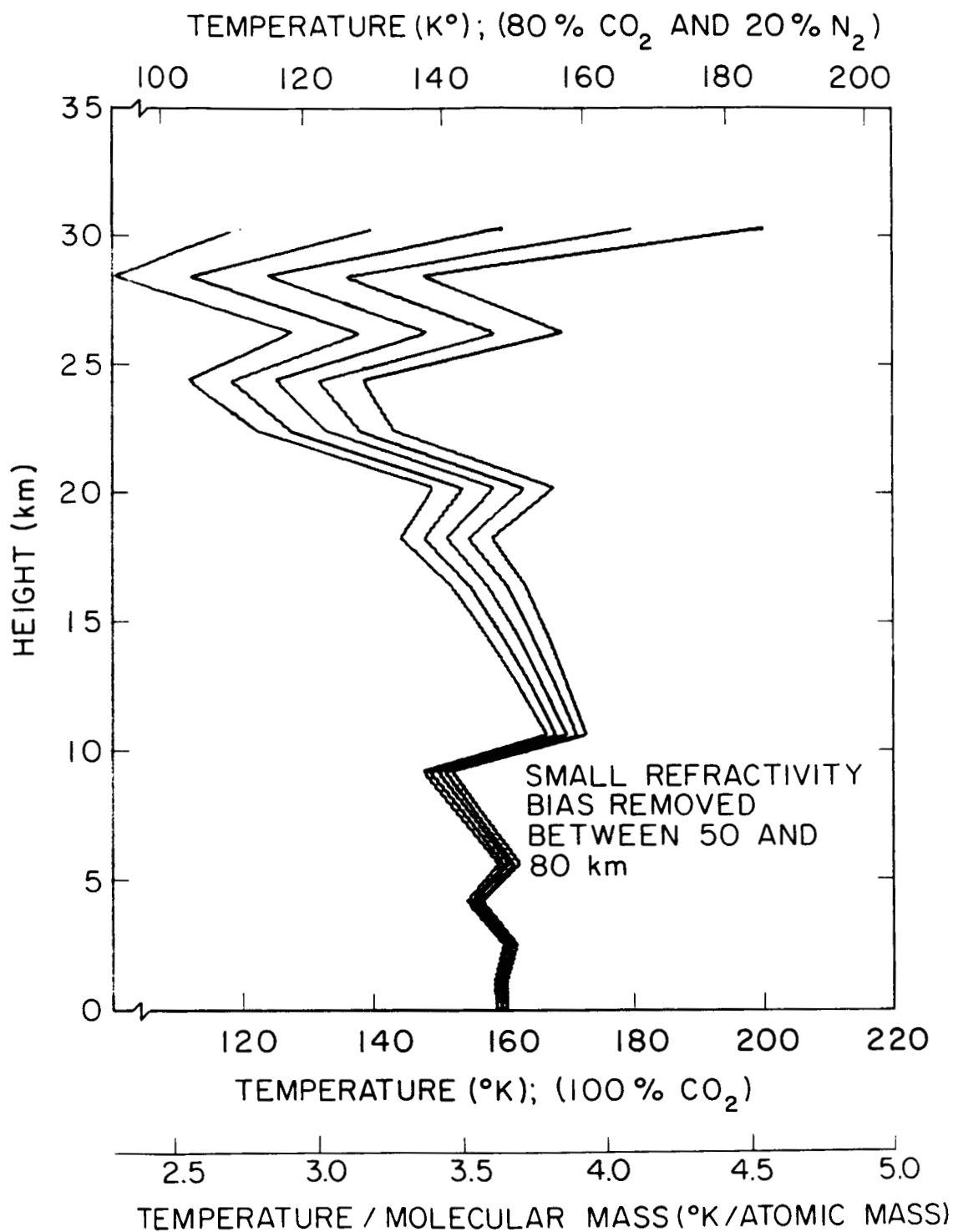


FIG. 10. TEMPERATURE PROFILES FOR THE LOWER ATMOSPHERE PROBED DURING IMMERSION. The temperature to mean molecular mass ratio is independent of the assumed composition.

By increasing the nitrogen abundance, one reduces the mean molecular mass which again reduces the temperature computed from Eq. 11.

In order to have a stable atmosphere near the surface, it is necessary for the temperature to be equal to or greater than the saturation temperature for CO_2 vapor. This constraint provides an upper limit of about 20% for the N_2 abundance in the lower atmosphere over Electris.

The emersion results are shown in Figure 11. The two sets of profiles denoted I and II were obtained from the corresponding number density profiles shown in Fig. 8 and 9. The five boundary temperatures were chosen near 33 km altitude.

The temperature peak near 10 km altitude in Fig. 11 is produced by the dip in the refractivity profile associated with the change from one-way to two-way mode of operation. Thus, the peak in the computed temperature profile was probably produced by changes in the radio system rather than by a hot layer in the Martian atmosphere.

The temperature profiles obtained from the immersion and emersion measurements show that the Martian summer night at 60°N was considerably warmer than the winter day at 50°S latitude. The results suggest, furthermore, that the temperature lapse rate may be decreasing with increasing solar latitude. These effects are also observed in the terrestrial atmosphere and they are confirmed by theoretical model studies of the Martian atmosphere (Leovy, 1966; Leovy and Mintz, 1966; Ohring and Mariano, 1967).

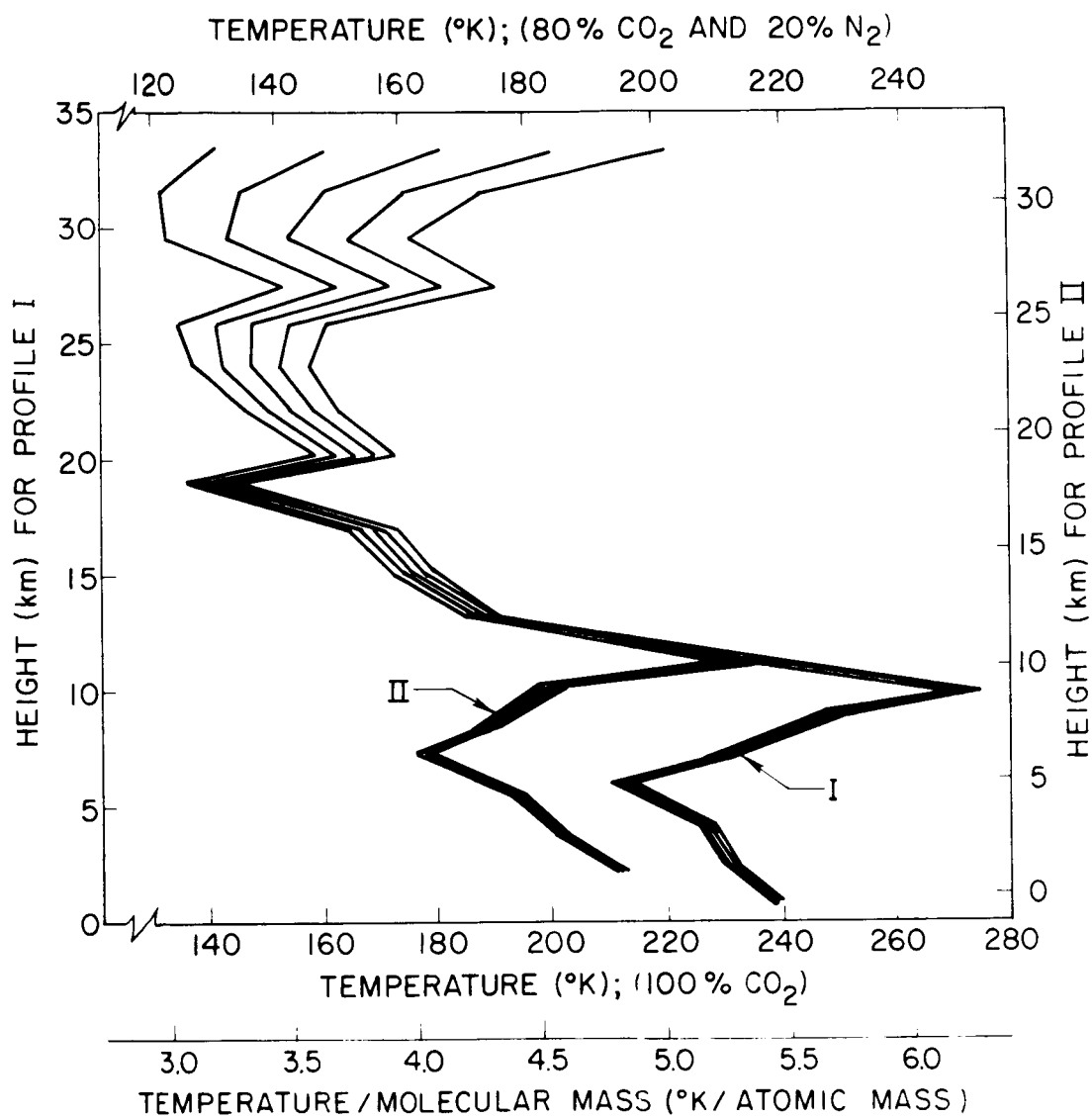


FIG. 11. TEMPERATURE PROFILES FOR THE LOWER ATMOSPHERE PROBED DURING EMERSION.

Utilizing Eq. (9), one can determine the pressure profiles corresponding to the various temperature and number density profiles. The results are shown in Figure 12. The pressure for emersion is seen to be substantially higher than for immersion. The pressure difference corresponds to a gravitational equipotential altitude difference on the order of 6 to 9 km between the two occultation points. (It is also possible that local high and low pressure regions may have contributed to the observed differences)

The radius (measured from the Martian center of mass) may also have differed at the two occultation points. Kliore et al (1966) reported that the radius at the immersion point (in the bright area Electris) was from -2 to +12 km larger than at the emersion point (near the northern border of Mare Acidalius). Our own calculations yield similar values.⁺

+ Pettengill has recently utilized variations in the time of arrival of the leading edge of pulsed monostatic radar echoes to study topographic elevation differences near the 21° north latitude circle on Mars (Pettengill 1967). He found altitude variations as large as 11 km at this latitude. (Individual altitude measurements represent an average over about a 200 km diameter circle on Mars, so that peak variations are no doubt greater). Pettengill's data also indicate that the dark maria tend to be located at lower elevations than the bright areas. The findings of the radio occultation experiment seem to agree with this order of magnitude for the altitude difference and the correspondence of altitude with surface markings.

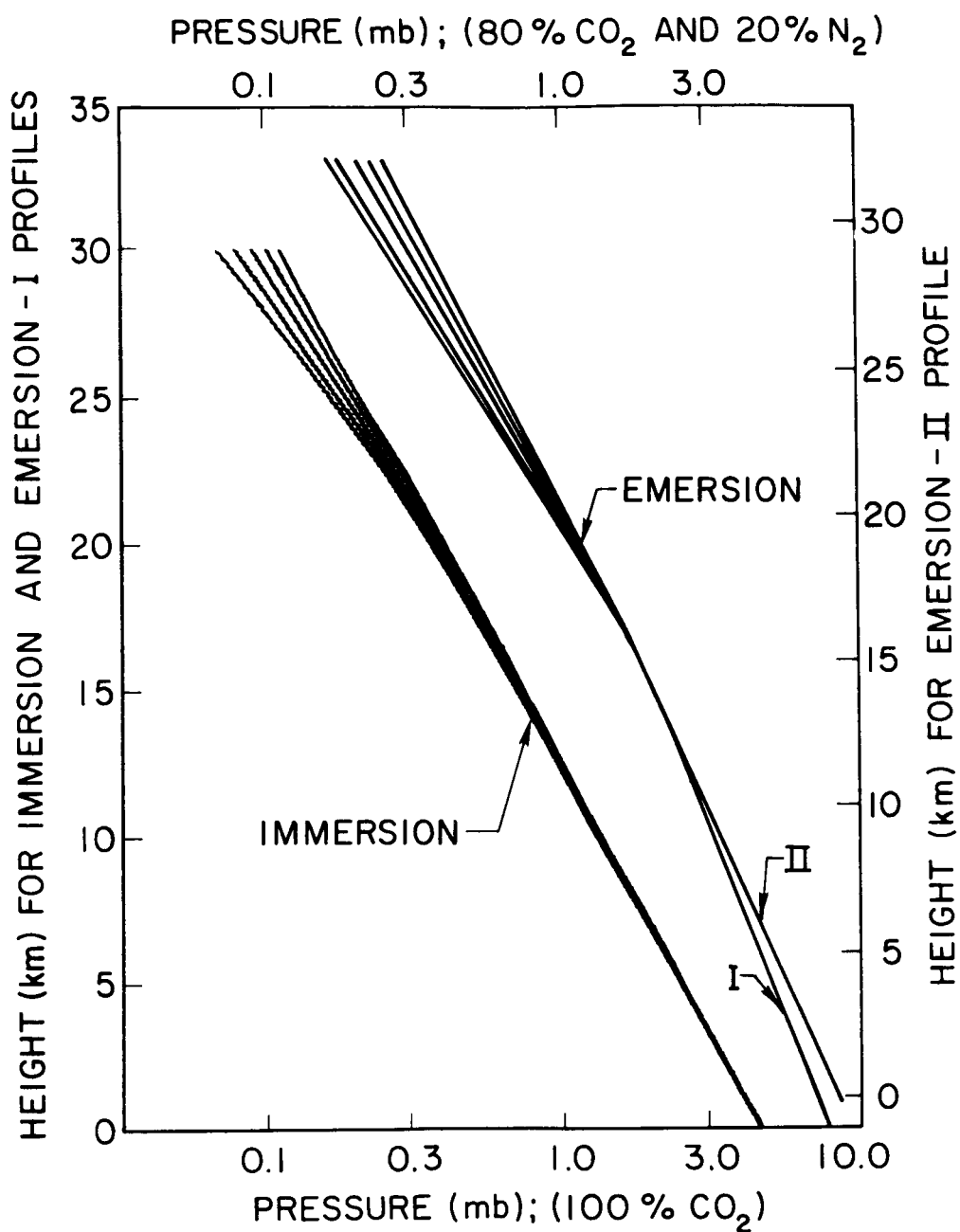


FIG. 12 PRESSURE PROFILES FOR IMMERSION AND EMERSION. The atmospheric pressure at the occultation level was 4.5 and about 8 mb for immersion and emersion, respectively.

The differences between the temperatures, pressures, and radii measured at the two occultation points are, of course, very interesting. However, it would be much more useful for detailed study and understanding to have many more than just two sets of atmospheric profiles. This need for repeated measurements at many different locations, times and seasons points to the use of planetary orbiters in future experiments of this type.

4. THE UPPER ATMOSPHERE OF MARS

From the magnetoionic theory, one can show that, for the conditions of this experiment, the refractivity N of free electrons is given by:

$$N = -40.3 \times 10^6 \frac{n_e}{f^2} \quad (12)$$

where n_e is the electron number density (m^{-3}) and f is the radio frequency (hertz). By employing this formula, one can convert the refractivity measurements in the upper atmosphere over Electris into electron number densities. The resulting electron number density profile is shown in Fig. 13.

Assuming that the ionospheric topside is in ambipolar diffusive equilibrium, one can show that the plasma temperature T_p in this region is given by:

$$T_p(h) = T_p(h_o) \cdot \frac{N(h_o)}{N(h)} + \frac{m_i}{2kN(h)} \int_h^{h_o} g(h) N(h) dh \quad (13)$$

where m_i denotes the mass of the principal ion. The other symbols involved were defined in Sec. 3 (cf. Eq. 11).

Figure 14 shows the plasma temperature profiles obtained by integrating Eq. (13) downward from 220 km altitude. The ion mass was assumed to be constant and independent of altitude in these calculations.

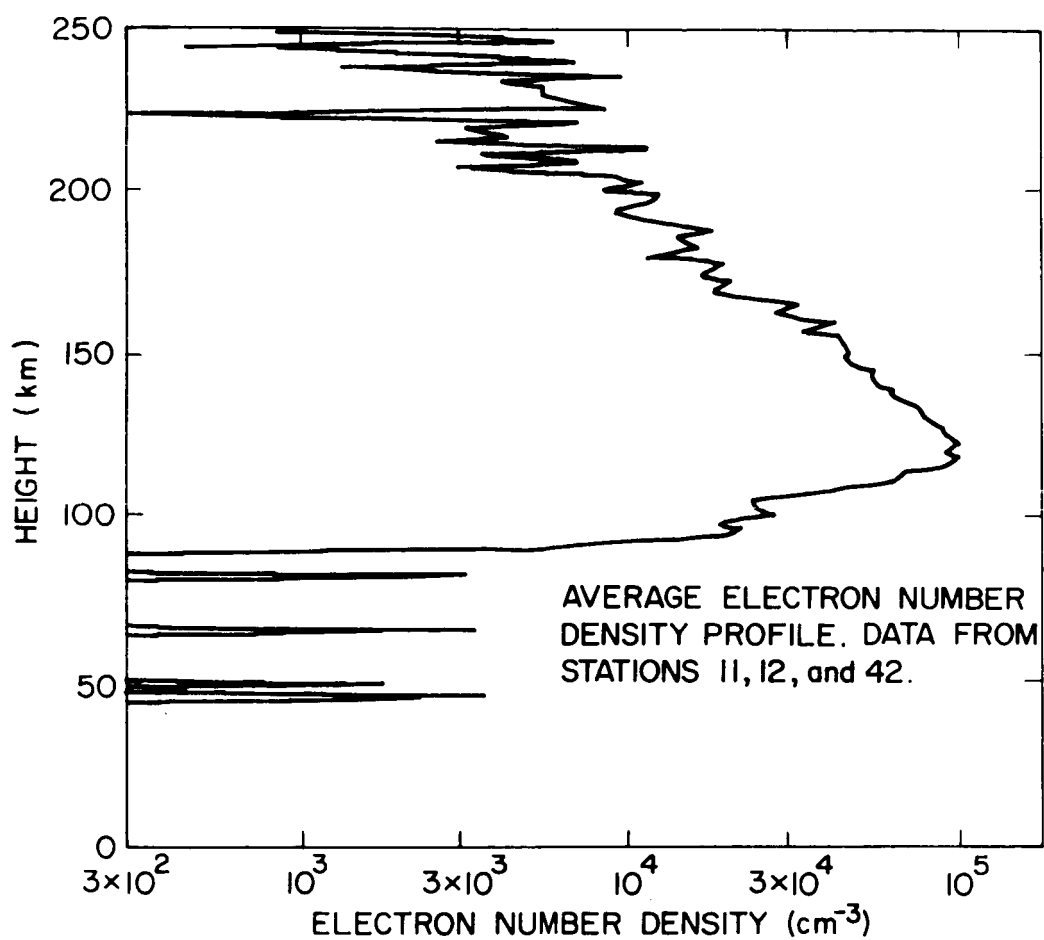


FIG. 13. ELECTRON NUMBER DENSITY PROFILE FOR THE UPPER ATMOSPHERE PROBED DURING IMMERSION. 50° S latitude, 177° E longitude, 1300 hours local time, late winter, solar zenith angle 67°.

We do not know what the principal ion is on the topside of the Martian ionosphere. Possible candidates include CO_2^+ , O^+ , and a number of ions of intermediate mass. In order to illustrate the effect of this uncertainty, Fig. 14 has been provided with three different temperature scales corresponding to an ion mass of 44 (CO_2^+), 32 (O_2^+), and 16 (O^+).

Refractivity bias between 280 and 380 km altitude was calculated and subtracted from the rest of the profile before the plasma temperature was determined. In order to establish how the uncertainties in the bias affect the results, we analyzed the refractivity profiles determined from doppler data obtained prior to occultation. These profiles were divided into layers of 80 km thickness (approximately the depth of the ionospheric topside) and the average refractivity was computed for each layer. The standard deviation of the difference between the average refractivities of layers separated in altitude by 80 km was found to be about 0.01 refractivity units ($1.3 \times 10^3 \text{ elec/cm}^3$). A change in the entire topside refractivity profile of ± 0.01 resulted in a $\pm 4\%$ change in the plasma temperature near 130 km altitude.

The temperature profiles shown in Fig. 14 are based on the assumption that the ionospheric topside is in ambipolar diffusive equilibrium. We have also made calculations for the case of a Chapman layer in photoionization equilibrium. Assuming that the ionization cross section and the electron recombination coefficient are independent of altitude, these calculations yield temperature

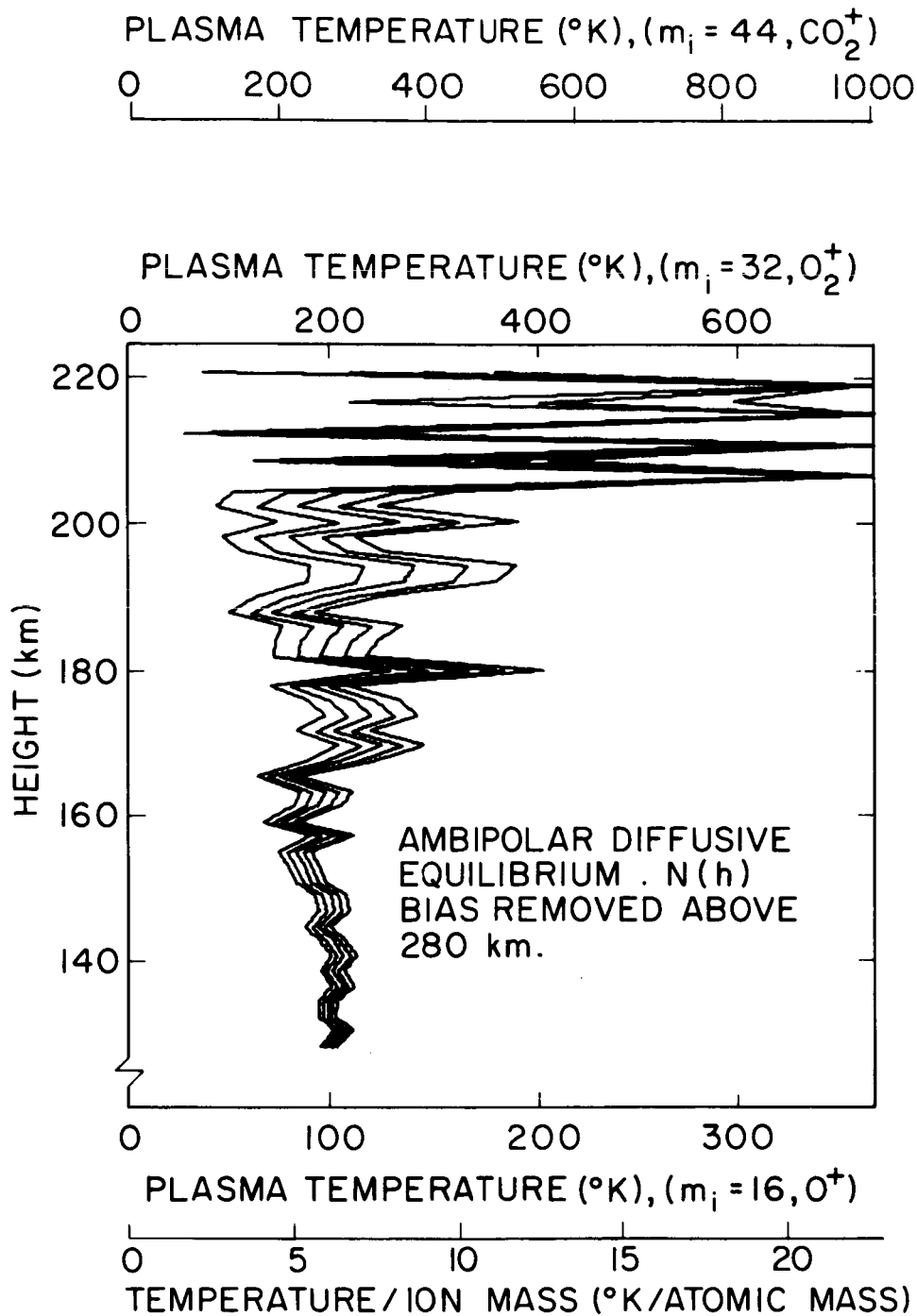


FIG. 14. PLASMA TEMPERATURE PROFILES FOR THE UPPER ATMOSPHERE PROBED DURING IMMERSION. Refractivity bias removed above 280 km altitude.

profiles similar to those shown in Fig. 14 except that the temperatures near the ionization peak are lower.

The interpretation of the immersion measurements has led to three different types of models for the atmosphere of Mars. By analogy with the ionization regions formed in the terrestrial atmosphere, one can denote these three classes of models: F_2 , F_1 , and E.

The F_2 (or Bradbury) models are based on the assumption that the observed ionization peak was produced by a rapid decrease of the ion recombination loss coefficient with increasing altitude, combined with downward plasma diffusion. In these models, the ionization peak is formed above the region where most of the ion production and recombination takes place. The F_1 and E (or Chapman) models rest on the assumption that the observed ionization peak coincides with the ion production peak caused by extreme solar ultraviolet and X-rays, respectively.

The full-drawn curves in Figs. 15 and 16 show the number density and temperature profiles of one of the F_2 models that have been proposed for the Martian atmosphere. In this model, CO_2 is dissociated into CO and O by solar ultraviolet. It is assumed that diffusive equilibrium prevails above the dissociation region and that atomic oxygen predominates in the upper atmosphere.

The atomic oxygen density at the ionization peak (10^9 cm^{-3}) was estimated by equating the photoionization rate and the rate of downward plasma diffusion. The carbon dioxide density at this

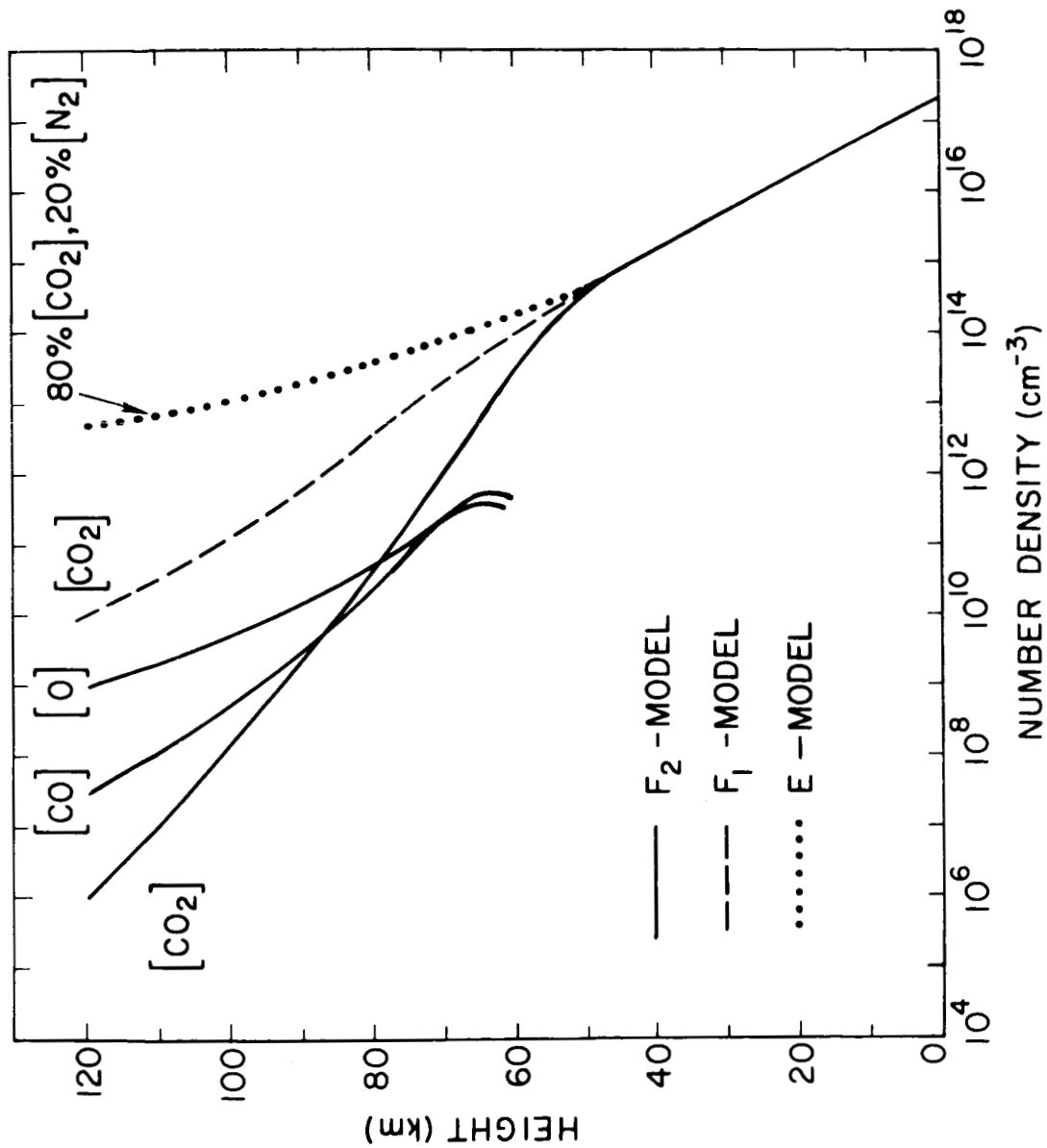


FIG. 15. NUMBER DENSITY VERSUS ALTITUDE FOR THREE DIFFERENT ATMOSPHERIC MODELS. The profiles apply to the immersion measurements.

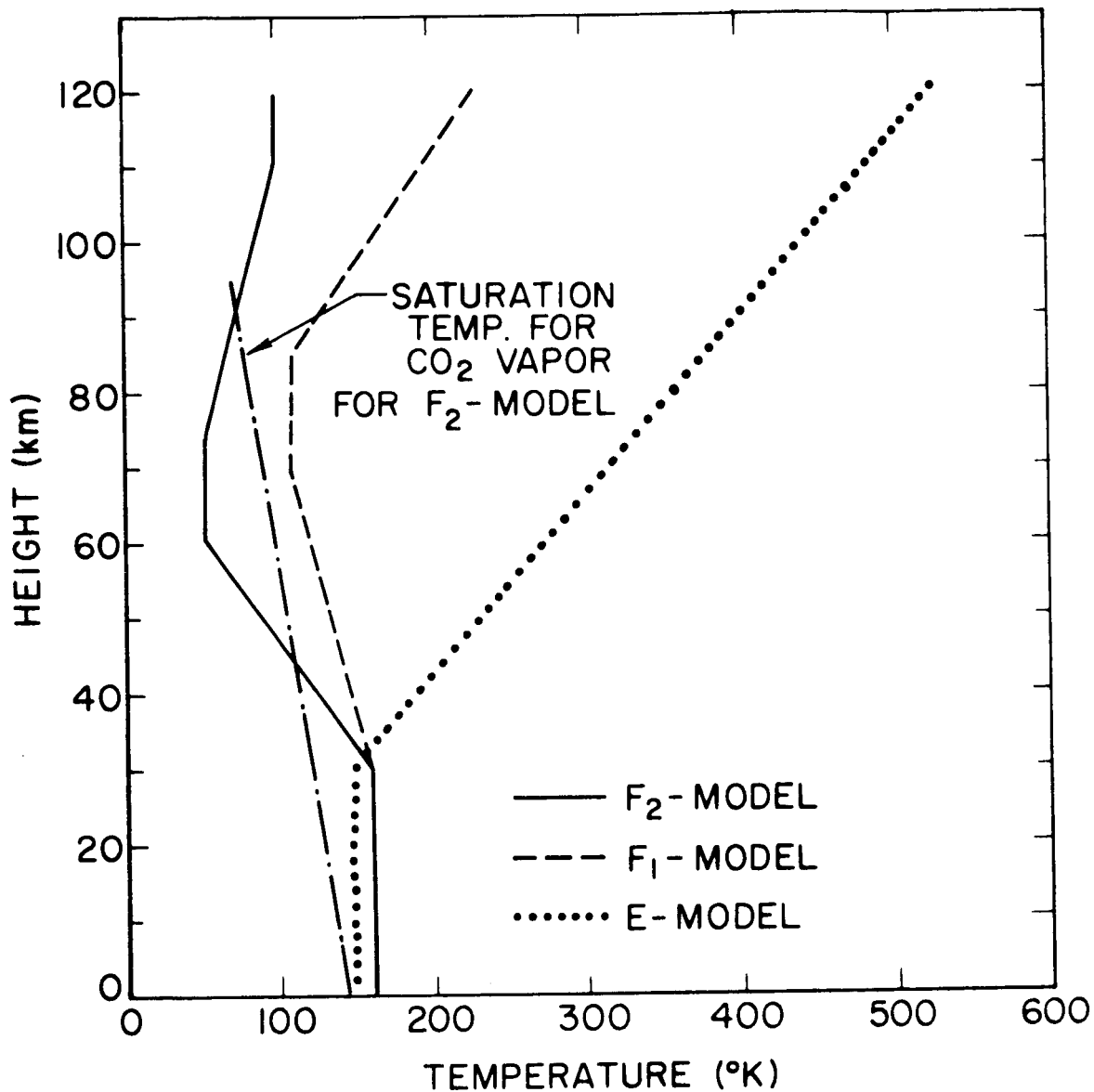


FIG. 16. TEMPERATURE VERSUS ALTITUDE FOR THREE DIFFERENT ATMOSPHERIC MODELS. The profiles apply to the immersion measurements.

altitude (10^6 cm^{-3}) was determined by equating the rates of diffusion and electron recombination loss. The limiting ion loss process at the ionization peak is assumed to be $\text{O}^+ + \text{CO}_2 \rightarrow \text{O}_2^+ + \text{CO}$ with a rate coefficient of $10^{-9} \text{ cm}^3/\text{sec}$ (Fehsenfeld et al, 1966). A more detailed description of this F_2 model has been given by Fjeldbo et al (1966). Another F_2 model has been offered by Johnson (1965).

The main difficulty with the proposed F_2 models is the low atmospheric temperatures that they require. If O^+ were the principal ion on the topside of the Martian ionosphere, the plasma temperature would only be about 100° K (cf. Fig. 14) in this region of the atmosphere and the temperature of the neutral gas would probably have to be even lower.

A number of investigators have worked on thermal model studies of the Martian upper atmosphere (Chamberlain and McElroy, 1966; Fjeldbo et al, 1966; Gross et al, 1966; Smith and Beutler, 1966). These theoretical estimates yield higher temperatures than 100° K on the ionospheric topside--which indicates that the principal ion in this region is heavier than O^+ (cf. Fig. 14). One should keep in mind, however, that these temperature estimates are subject to considerable uncertainty due to simplifying assumptions, the omission of possibly important processes, and poorly-known parameters (Johnson, 1966; Fjeldbo and Eshleman, 1967). Thus, it appears difficult to draw definite conclusions based on these model studies.

If the Martian upper atmosphere is composed mainly of molecular constituents such as CO_2 , CO , or O_2 , the ionization peak may coincide with the ion production peak caused by extreme solar ultraviolet (Donahue, 1966; Fjeldbo et al, 1966). The dashed curves in Figs. 15 and 16 show an example of such a model. It is based on the assumption that CO_2 is the major constituent both in the upper and the lower atmosphere of Mars. In this model, the ionization peak occurs at a neutral density of about 10^{10} molecules/cm³, where the slant optical depth in the extreme ultraviolet is unity.

An E model for the Martian atmosphere has been offered by Chamberlain and McElroy (1966). In their model the ionization peak observed with Mariner IV occurs at a neutral density of 5×10^{12} molecules/cm³.

Figures 15 and 16 show an example of an E model. It has the same total number density at 120-km altitude as proposed by Chamberlain and McElroy but the temperature profile and the composition^ω have been altered in order to obtain a model that is compatible with the refractivity measurements made in the lower atmosphere over Electris.

The straight-line (E model) temperature profile shown between 30 and 120 km altitude in Fig. 16 is not based on any thermal study of this region of the atmosphere. It simply represents an extrapolation of the measurements made below 30 km altitude. The temperature

ω The composition was changed from 44% CO_2 and 56% N_2 to 80% CO_2 and 20% N_2 in order to avoid supersaturation of carbon dioxide vapor near the surface (cf. Sec. III and Fig. 10).

gradient above 30 km altitude was determined by requiring a number density of 5×10^{12} molecules/cm³ at 120 km altitude.

One difficulty with the E model illustrated in Figs. 15 and 16 is that it requires higher temperatures between the density levels 5×10^{12} cm⁻³ and 10^{15} cm⁻³ than suggested by the theoretical temperature computations (Prabhakara and Hogan, 1965; Chamberlain and McElroy, 1966; Smith and Beutler, 1966; Fjeldbo and Eshleman, 1967). Other problems arise when one attempts to explain the absence of an F₁ layer above 120 km altitude (Fjeldbo et al, 1966).

The three classes of atmospheric models that have been reviewed here yield atmospheric number densities that differ by almost four orders of magnitude at 120 km altitude. It may not be possible to resolve this uncertainty before other independent evidence becomes available. Ultraviolet detection of ionospheric constituents might be particularly valuable. It might also be worthwhile to improve the radio occultation measurements. One could, for example, increase the sensitivity of the electron number density measurements by employing one or more lower frequencies (in addition to the tracking and telemetry signal). Absorption measurements at these lower frequencies would, moreover, enable us to estimate the vertical electron collision frequency profile in the lower ionosphere of Mars (Fjeldbo et al, 1965). The collision frequency is again related to the temperature and density of the neutral gas--quantities of particular interest in the current debate on atmospheric models.

5. CONCLUSIONS

Our principal aim here was to present the results of the best analysis we could make of the basic data, with a minimum number of assumptions and interpretations. For example, the refractivity profiles for the lower atmosphere, and the electron number density profile for the upper atmosphere, were obtained by inversion of the measured phase data without smoothing to remove either radio or digitizing noise. The main difficulty here was in coping with the effects of our less than perfect knowledge of the spacecraft trajectory. The manner in which this problem was handled is explained in some detail.

From the refractivity profiles the molecular number density profiles follow if the constituents are assumed. Fortunately, there is very little latitude here, since the atmosphere appears to consist primarily of CO_2 . The two models considered--one of 100% CO_2 and the other 80% CO_2 with 20% N_2 --are thought to lead to reasonable limits to the probable uncertainties in number density, temperature, and pressure profiles due to unknown constituents. These two models differ by only 9% in molecular number density. The lower atmospheric profiles representing temperature divided by mean molecular mass were derived from the refractivity profiles, assuming only mixed, non-polar molecules in hydrostatic equilibrium. Different boundary conditions near 30 km altitude were used to start integrating downward to find the temperature over mass profiles, and it is apparent that the profiles below about 20 kilometers are remarkably independent of the boundary condition. Ambipolar diffusive or photoionization equilibrium conditions

were assumed in deriving, in a similar manner, profiles which represent the plasma temperature divided by mean ionic mass for the upper atmosphere. Pressure profiles were derived for the lower atmosphere from the number density and temperature profiles. The two models considered have only a 1% pressure difference due to different constituents. A large pressure difference was found between immersion and emersion, and this is attributed primarily to a difference in altitude of the occulting features.

APPENDIX A

Raypath Approximations

The purpose of this appendix is to verify some of the approximations utilized in Section 2. The geometry is illustrated in Fig. 17 where s denotes the raypath between the earth and the spacecraft and l_1 and l_2 denote the length of the corresponding raypath asymptotes. The phase path increase (ϕ) produced by the planetary atmosphere is given by

$$\phi = \frac{1}{\lambda} \int_{\text{along ray path}} [1 + 10^{-6} N(\rho)] ds - \frac{l_1 \cos(\delta_s - \delta) + l_2 \cos(\alpha + \delta - \delta_s)}{\lambda} \quad (\text{cycles}) \quad (\text{A1})$$

where $l_1 \cos(\delta_s - \delta) + l_2 \cos(\alpha + \delta - \delta_s)$ is the distance between the tracking station and the spacecraft, and λ is the free space wavelength. The atmospheric refractivity $N(r)$ is assumed to be a function only of the distance to the center of the planet (r) .

Utilizing Bouger's rule [Born and Wolf, (1959)], we have

$$a = \rho [1 + 10^{-6} N(\rho)] \quad (\text{A2})$$

where ρ and a are the radii of closest approach for the raypath and its asymptotes, respectively. Employing Eq. (A2), one can show that

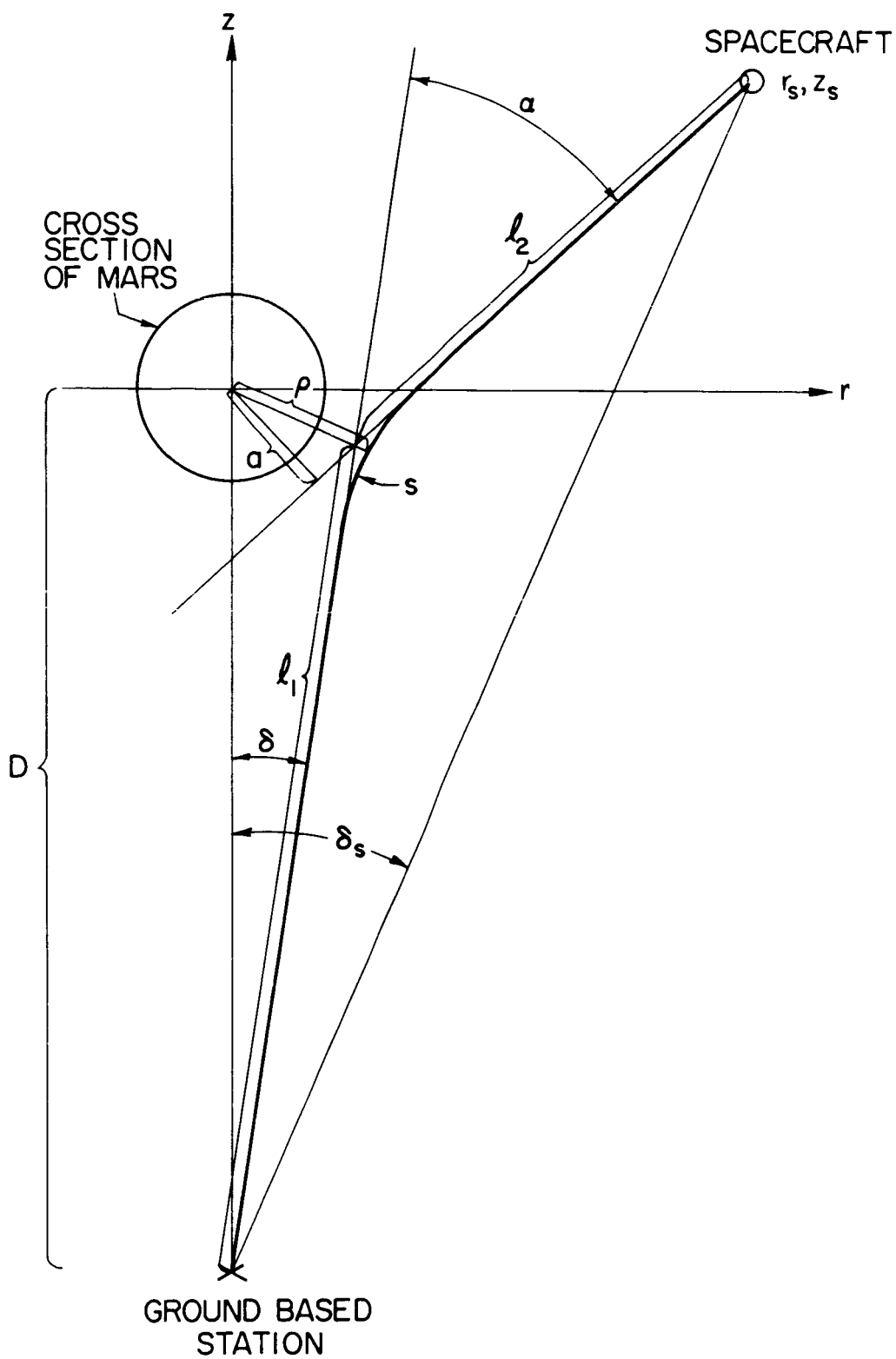


FIG. 17. RAY PATH GEOMETRY. Mars was at a distance of 216 million kilometers from the earth during the measurements.

$$\rho = \frac{r_s \cos(\alpha+\delta) - z_s \sin(\alpha+\delta)}{1 + 10^{-6} N(\rho)} \quad (A3)$$

and that

$$\ell_2 = \frac{z_s}{\cos(\alpha+\delta)} + \frac{\rho \sin\left(\frac{\alpha}{2} + \delta\right)}{\cos(\alpha+\delta) \cos\left(\frac{\alpha}{2}\right)} [1 + 10^{-6} N(\rho)] \quad (A4)$$

where r_s and z_s are the spacecraft coordinates.

Equations (A1) through (A4) are general formulations that apply to any ray passing through a spherically symmetric medium. These equations can be simplified considerably when applied to propagation in the Martian atmosphere. For example, one can omit the term $10^{-6} N(\rho)$ in the expression for ρ because the maximum value of this term is only about 4×10^{-6} . The maximum errors introduced in ρ by this approximation is of the order of 10 meters which is only about 0.1% of the atmospheric scale height.

Similarly, one can simplify the terms involving $(\alpha+\delta)$, because the magnitude of this angle did not exceed 0.0002 radians. Terms of second and higher order in $(\alpha+\delta)$ contributed less than 10 meters to the value of ρ . Thus, we have:

$$\rho = r_s - z_s (\alpha+\delta) \quad (A5)$$

where δ is given to first order by $\delta = r_s/D$. We have, therefore, verified Eq. (2) of Section 2.

Similarly, one can simplify Eq. (A1)

$$\phi = \phi_1 + \frac{\ell_1}{2\lambda} (\delta_s - \delta)^2 + \frac{\ell_2}{2\lambda} (\alpha + \delta - \delta_s)^2 \quad (\text{A6})$$

where

$$\phi_1 = \frac{1}{\lambda} \int_{\text{along ray path}} [1 + 10^{-6} N(\rho)] ds - \frac{\ell_1 + \ell_2}{\lambda} \quad (\text{A7})$$

For small banding, Eq. (6) and (A7) are equivalent. Terms containing $(\delta - \delta_s)$ can be neglected in Eq. (A6). This simplification yields

$$\phi = \phi_1 + \frac{\ell_2}{2\lambda} \alpha^2 \quad (\text{A8})$$

Utilizing Eq. (A4), one can show that it makes negligible difference in the phase path ϕ when ℓ_2 is replaced by z_s . Thus, we have

$$\phi = \phi_1 + \frac{z_s \alpha^2}{2\lambda} \quad (\text{A9})$$

which is the same as Eq. (5) of Section 2.

APPENDIX B

A Procedure for Calculation of $N(r)$ from $\phi_1(\rho)$

In this appendix, we discuss in greater detail how to invert Eq. (6) to obtain $N(r)$. The procedure to be outlined here is based on the assumption that the atmosphere is spherically symmetric. When applied to a real atmosphere, this procedure yields a "mean refractivity profile" where the horizontal gradients have been averaged out.*

The geometry is illustrated in Fig. 18 where K rays are passing through an atmosphere consisting of K spherical layers. Each atmospheric layer has constant refractivity and constant thickness.

It is here convenient to replace Eq. (6) of Section II by a system of K linear equations of the form:

$$\lambda 10^6 \phi_1(m) = N(m)\Delta z(m,m) + 2 \sum_{n=1}^{m-1} N(n)\Delta z(m,n) \quad (B1)$$

where $\phi_1(m)$ denotes ϕ_1 for the m^{th} ray and $N(n)$ is the refractivity in the n^{th} layer. The matrix element $\Delta z(m,n)$ designates the length of that portion of the m^{th} ray which lies within the n^{th} layer, as illustrated in Fig. 18.

*The procedure described here can also be utilized to invert $\phi_1(\rho)$ when there are horizontal refractivity gradients in the atmosphere. However, the magnitude of the horizontal gradients must be assumed before one can compute the vertical gradients [Fjeldbo, 1964].

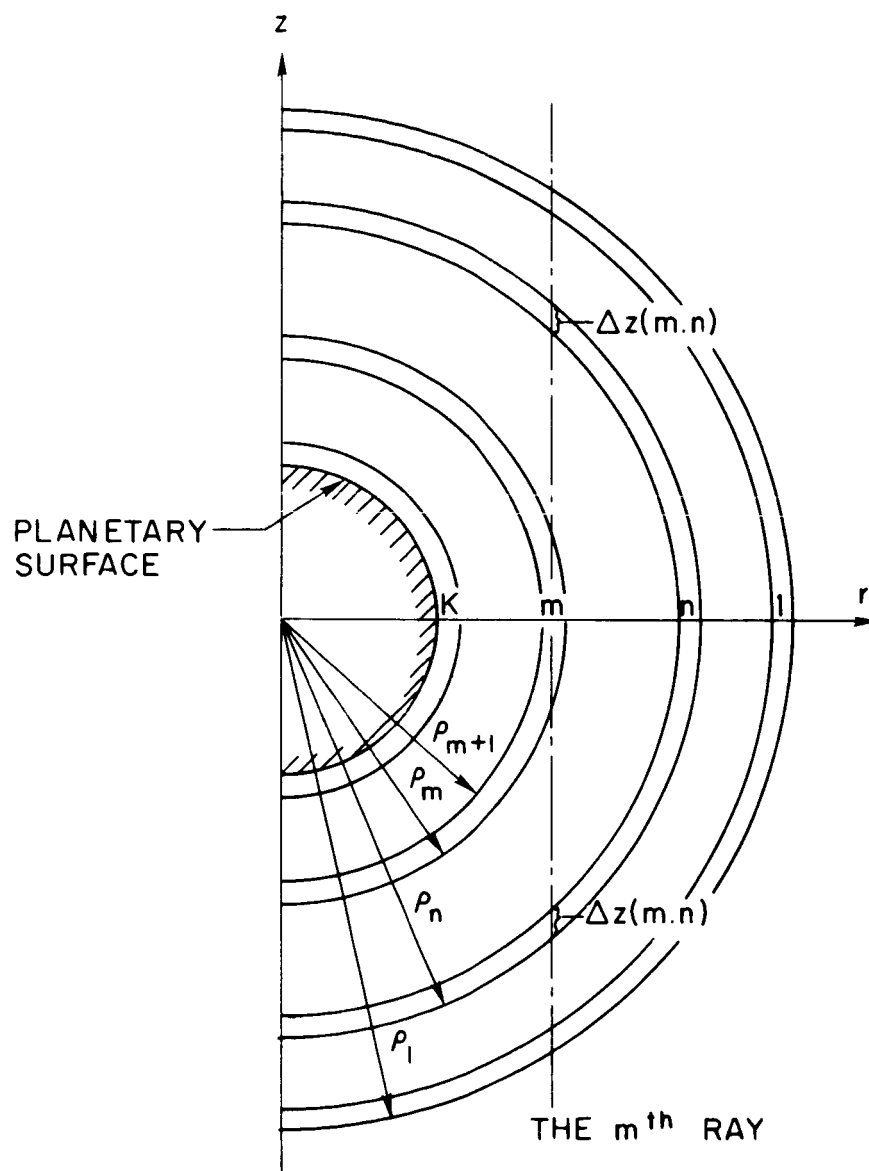


FIG. 18. CROSS SECTION OF ATMOSPHERE CONSISTING OF K SPHERICAL LAYERS.

The two dimensional matrix Δz is related to the radii of the atmospheric layers by:

$$\Delta z(m,n) = \left[\rho_n^2 - \left(\frac{\rho_m + \rho_{m+1}}{2} \right)^2 \right]^{1/2} - \left[\rho_{n+1}^2 - \left(\frac{\rho_m + \rho_{m+1}}{2} \right)^2 \right]^{1/2} \quad (B2)$$

for $m > n$ and

$$\Delta z(m,m) = 2 \left[\rho_m^2 - \left(\frac{\rho_m + \rho_{m+1}}{2} \right)^2 \right]^{1/2} \quad (B3)$$

for $n = m$.

Solving Eq. (B1) with respect to N yields

$$N(1) = \lambda 10^6 \phi_1(1) / \Delta z(1,1)$$

$$N(2) = \left[\lambda 10^6 \phi_1(2) - 2 \sum_{n=1}^1 N(n) \Delta z(2,n) \right] / \Delta z(2,2)$$

$$N(m) = \left[\lambda 10^6 \phi_1(m) - 2 \sum_{n=1}^{m-1} N(n) \Delta z(m,n) \right] / \Delta z(m,m) \quad (B4)$$

which provides us with a recursive formulation relating N explicitly to ϕ_1 .

The inversion procedure described in this report is based on the assumption that the refraction is small. This approach does not apply to Venus and the Jovian planets whose atmospheres are several orders of magnitude denser than that of Mars. A more general procedure has been developed for handling these cases and it will be employed in the analysis of the Mariner V - Venus (1967) data.

REFERENCES

- Belton, Michael J. S., and Donald M. Hunten, "The Abundance and Temperature of CO₂ in the Martian Atmosphere," Ap. J., 145, 454, No. 2, 1966.
- Born, M. and E. Wolf, "Principles of Optics," Pergamon Press, New York, 1959.
- Chamberlain, J. W., and M. B. McElroy, "The Martian Atmosphere: An Interpretation of the Mariner Occultation Experiment," Science, 152, 21, 1966.
- Donahue, T. M., "Upper Atmosphere and Ionosphere of Mars," Science, 152, 763-764, 1966.
- Essen, L., K. D. Froome, "The Refractive Indices and Dielectric Constants of Air and its Principal Constituents at 24,000 Mc/s," Proc. Phys. Soc., London, B, 64, 862-875, 1951.
- Fehsenfeld, F. S., E. E. Ferguson, A. L. Schmeltekopf, "Thermal-Energy Ion-Neutral Reaction Rates III. The Measured Rate Constant for the Reaction $O^+(^4S) + CO_2(^1\Sigma) \longrightarrow O_2^+(^2II) + CO(^1\Sigma)$," J. Chem. Phys., 44, 3022-4, 1966.
- Fjeldbo, G., "Bistatic-Radar Methods for Studying Planetary Ionospheres and Surfaces," Sci. Rpt. No. 2, NsG-377, SU-SEL-64-025, Stanford Electronics Laboratories, Stanford, California, April, 1964.
- Fjeldbo, G., V. R. Eshleman, "The Atmosphere of Mars: Radio Occultation Measurements and Interpretations," Proc. Conf. on the Atmos. of Mars and Venus, Tucson, Arizona, Feb. 28-Mar. 2, 1967.
- Fjeldbo, G., and V. R. Eshleman, "The Bistatic Radar-Occultation Method for the Study of Planetary Atmospheres," J. Geophys. Res., 70, 3217-3226, 1965.
- Fjeldbo, G., V. R. Eshleman, O. K. Garriott, F. L. Smith, III, "The Two Frequency Bistatic Radar-Occultation Method for the Study of Planetary Ionospheres," J. Geophys. Res., 70, Aug., 1965.
- Fjeldbo, G., W. C. Fjeldbo, V. R. Eshleman, "Atmosphere of Mars: Mariner IV Models Compared," Science, 153, 1518-1523, Sept., 1966.
- Gross, S. H., W. E. McGovern, S. I. Rasool, "Mars: Upper Atmosphere," Science, 151, 1216-1221, 1966.
- Harrington, J. W., M. D. Grossi, B. M. Langworthy, "Mars Mariner IV Radio Occultation Experiment: Comments on the Uniqueness of the Results," in press.

Johnson, F. S., "Atmosphere of Mars," Science, 150, 1445-1448, Dec., 1965.

Johnson, F. S., "The Atmosphere of Mars," presented at 7th Internat. Space Sci. Symp., Comm. on Space Res., (COSPAR), Vienna, Austria, May 11-17, 1966.

Kliore, A., D. L. Cain, G. S. Levy, "Radio Occultation Measurement of the Martian Atmosphere over Two Regions by the Mariner IV Space Probe," presented at 7th Internat. Space Sci. Symp., Comm. on Space Res., (COSPAR), Vienna, Austria, May 11-17, 1966.

Kliore, A., D. L. Cain, G. S. Levy, V. R. Eshleman, G. Fjeldbo, F. D. Drake, "Occultation Experiment: Results of the First Direct Measurement of Mars's Atmosphere and Ionosphere," Science, 149, 1243-1248, 1965.

Leovy, C. B., "Radiative-Convective Equilibrium Calculations for a Two-Layer Mars Atmosphere," RM-5017-NASA (NASr-21-07), The Rand Corp., Santa Monica, California, May 1966.

Leovy, C. B., Y. Mintz, "A Numerical General Circulation Experiment for the Atmosphere of Mars," RM-5110-NASA (NASr-21-07), The Rand Corp., Santa Monica, California, Dec. 1966.

Levy, G. S., T. Y. Otoshi, B. L. Seidel, "Ground Instrumentation for Mariner IV Occultation Experiment," Tech. Rpt. No. 32-984, Jet Propulsion Laboratory, Pasadena, California, Sept., 1966.

Ohring, G., W. Tang, J. Mariano, "Planetary Meteorology, Final Rpt. NASW-1227, GCA-TR-67-5-N, GCA Corp., Bedford, Mass., March, 1967.

Pettengill, G. H., paper presented before the 13th General Assembly of the International Astronomical Union, Prague, 22-31 August 1967.

Prabhakara, C., J. S. Hogan, Jr., "Ozone and Carbon Dioxide Heating in the Martian Atmosphere," J. Atmos. Sci., 22, 97-109, 1965.

Rea, D. G., "The Atmosphere and Surface of Mars--A Selective Review," Proc. of the Caltech-JPL Lunar and Plan. Conf., Sept. 13-18, Jet Propulsion Laboratory, Pasadena, Calif., 209-238, 1965.

Smith, N., A. Beutler, "A Model Martian Atmosphere and Ionosphere," Rpt. 66-3, Univ. of Michigan Radio Astron. Observ., Ann Harbor, Mich., March, 1966.

Spinrad, Hyron, Ronald A. Schorn, Roger Moore, L. P. Giver, and H. J. Smith, "High-Dispersion Spectroscopic Observations of Mars I." The CO₂ Content and Surface Pressure, Ap. J., 146, 33, Nov. 1966.